

Three-body unitary coupled-channel approach to radiative J/ψ decays and $\eta(1405/1475)$ S. X. Nakamura^{1,2,3,*} Q. Huang,⁴ J.-J. Wu^{5,†} H. P. Peng,^{2,3} Y. Zhang^{2,3} and Y. C. Zhu^{2,3}¹*Institute of Frontier and Interdisciplinary Science, Shandong University, Qingdao, Shandong 266237, China*²*University of Science and Technology of China, Hefei 230026, China*³*State Key Laboratory of Particle Detection and Electronics (IHEP-USTC), Hefei 230036, China*⁴*Department of Physics, Nanjing Normal University, Nanjing, Jiangsu 210097, China*⁵*School of Physical Sciences, University of Chinese Academy of Sciences (UCAS), Beijing 100049, China*

(Received 15 November 2023; accepted 14 December 2023; published 19 January 2024)

Recent BESIII data on radiative J/ψ decays from $\sim 10^{10}$ J/ψ samples should significantly advance our understanding of the controversial nature of $\eta(1405/1475)$. This motivates us to develop a three-body unitary coupled-channel model for radiative J/ψ decays to three-meson final states of any partial wave (J^{PC}). Basic building blocks of the model are bare resonance states such as $\eta(1405/1475)$ and $f_1(1420)$, and πK , $K\bar{K}$, and $\pi\eta$ two-body interactions that generate resonances such as $K^*(892)$, $K_0^*(700)$, and $a_0(980)$. This model reasonably fits $K_S K_S \pi^0$ Dalitz plot pseudodata generated from the BESIII's $J^{PC} = 0^{-+}$ amplitude for $J/\psi \rightarrow \gamma K_S K_S \pi^0$. The experimental branching ratios of $\eta(1405/1475) \rightarrow \eta\pi\pi$ and $\eta(1405/1475) \rightarrow \gamma\rho$ relative to that of $\eta(1405/1475) \rightarrow K\bar{K}\pi$ are simultaneously fitted. Our 0^{-+} amplitude is analytically continued to find three poles, two of which correspond to $\eta(1405)$ on different Riemann sheets of the $K\bar{K}$ channel, and the third one for $\eta(1475)$. This is the first pole determination of $\eta(1405/1475)$ and, furthermore, the first-ever pole determination from analyzing experimental Dalitz plot distributions with a manifestly three-body unitary coupled-channel framework. Process-dependent $\eta\pi\pi$, $\gamma\pi^+\pi^-$, and $\pi\pi\pi$ lineshapes of $J/\psi \rightarrow \gamma(0^{-+}) \rightarrow \gamma(\eta\pi\pi)$, $\gamma(\gamma\rho)$, and $\gamma(\pi\pi\pi)$ are predicted, and are in reasonable agreement with data. A triangle singularity is shown to play a crucial role to cause the large isospin violation of $J/\psi \rightarrow \gamma(\pi\pi\pi)$.

DOI: [10.1103/PhysRevD.109.014021](https://doi.org/10.1103/PhysRevD.109.014021)**I. INTRODUCTION**

Since their first observation in 1967 [1], the light isoscalar pseudoscalar states in the 1.4–1.5 GeV region, named $\eta(1405/1475)$, have invited lots of debate about their peculiar features in experimental data and about various theoretical interpretations. There are two major open questions regarding $\eta(1405/1475)$: (i) are there one or two η excited states in this energy region?, and (ii) what is the internal structure of the excited state(s)? What makes $\eta(1405/1475)$ difficult to understand is that $\eta(1405/1475)$ could include various components such as a quark-antiquark pair, various hadronic coupled-channels, and a glueball, reflecting the complex nature of QCD in the low-energy regime. Also, the mixing between $(u\bar{u} + d\bar{d})/\sqrt{2}$ and $s\bar{s}$ is significant only in the isoscalar pseudoscalar sector.

Thus, understanding $\eta(1405/1475)$ seems particularly important for deepening our understanding of QCD.

$\eta(1405/1475)$ has been seen in various processes. However, the $\eta(1405/1475)$ lineshapes appear rather process different and thus have been explained with a single or two different states. For example, a single peak appears in $\eta\pi\pi$ final states from $p\bar{p}$ annihilation [2], radiative J/ψ decays [3–5], and $J/\psi \rightarrow \omega(\eta\pi\pi)$ [6] at somewhat process-dependent peak positions. A single peak is also found in $K\bar{K}\pi$ and $\eta\pi\pi$ final states from $\gamma\gamma$ collisions [7] and $\gamma\rho^0$ final states from radiative J/ψ decays [5,8,9] and $p\bar{p}$ annihilation [2]. On the other hand, structures seemingly due to two overlapping resonances are seen in $K\bar{K}\pi$ invariant mass distributions in π^-p scattering [10,11], $p\bar{p}$ annihilations [12], and radiative J/ψ decays [13,14].

The conventional quark model expects radially excited η and η' states in this energy region, and they correspond to $\eta(1295)$ and (one of) $\eta(1405/1475)$ states, respectively [15,16]. If $\eta(1405/1475)$ includes two states, what is its nature? A proposal was made to interpret $\eta(1405)$ as a glueball [17]. However, the isoscalar pseudoscalar glueball from lattice QCD (LQCD) predictions turned out to be significantly heavier [18–22]. Meanwhile, an LQCD prediction from Ref. [23] indicated only two states in this

*satoshi@sdu.edu.cn

†wujiajun@ucas.ac.cn

Published by the American Physical Society under the terms of the [Creative Commons Attribution 4.0 International license](https://creativecommons.org/licenses/by/4.0/). Further distribution of this work must maintain attribution to the author(s) and the published article's title, journal citation, and DOI. Funded by SCOAP³.

region. However, the authors did not identify them with $\eta(1295)$ and $\eta(1405/1475)$ since the experimental situation is unclear. Thus, although the two-state solution for $\eta(1405/1475)$ is not accommodated in the quark model, it is not forbidden by any strong theoretical arguments.

Another peculiar property of $\eta(1405/1475)$ is its anomalously large isospin violation in $\eta(1405/1475) \rightarrow \pi\pi\pi$ decays, as found in radiative J/ψ decays by the BESIII Collaboration in 2012 [24]. The BESIII Collaboration found that the decays mostly proceed as $\eta(1405/1475) \rightarrow f_0(980)\pi \rightarrow \pi\pi\pi$, and that the rate is significantly larger than that expected from $\eta(1405/1475) \rightarrow a_0(980)\pi$ followed by the $a_0(980)$ - $f_0(980)$ mixing. It was also found that the $f_0(980)$ width in the $\pi\pi$ invariant mass distribution is significantly narrower (~ 10 MeV) than those seen in other processes (~ 50 MeV) [15]. A theoretical explanation for these experimental findings was proposed in Refs. [25–28]. First, the authors pointed out that a $K^*\bar{K}K$ triangle loop from a $\eta(1405/1475)$ decay can hit an on-shell kinematics, causing a triangle singularity (TS) that can significantly enhance the amplitude. At the same time, this triangle loop causes the isospin violation due to the mass difference between K^\pm and K^0 in the $K^*K^-K^+$ and $K^*\bar{K}^0K^0$ triangle loops. This mechanism can naturally explain the large isospin violation without any additional assumptions.

The discovery of the potentially important TS effects in the $\eta(1405/1475)$ decays encouraged theorists to describe all $\eta(1405/1475)$ -related data, including process-dependent lineshapes, with one $\eta(1405/1475)$ state, based on the principle of Occam's razor [25–28]. Indeed, it was shown that the TS mechanisms can shift the resonant peak position somewhat, depending on $K\bar{K}\pi$, $\eta\pi\pi$, and $\pi\pi\pi$ final states. However, the experimental data of $K\bar{K}\pi$ and $\eta\pi\pi$ were rather limited at this time, and these theoretical results were not sufficiently tested. Also, it has not been possible to discriminate one- and two-state solutions of $\eta(1405/1475)$.

A significant advancement has been made recently by a BESIII analysis of $J/\psi \rightarrow \gamma(K_S K_S \pi^0)$ data from the high-statistics $\sim 10^{10}$ J/ψ decay samples [29]. They fitted the data with $J^{PC} = 0^{-+}, 1^{++}$, and 2^{++} partial-wave amplitudes, and identified two $\eta(1405/1475)$ states in the 0^{-+} amplitude with a high statistical significance.

However, there are theoretical issues in the BESIII analysis since they described the $\eta(1405/1475)$ states with Breit-Wigner (BW) amplitudes. The BW amplitude is known to be unsuitable in cases when a resonance is close to its decay channel threshold and/or when multiple resonances are overlapping [30]. This difficulty arises since the BW amplitude does not consider the unitarity. In the present case, $\eta(1405)$ is close to the $K^*\bar{K}$ threshold, and $\eta(1405)$ and $\eta(1475)$ are overlapping. Furthermore, while coupling parameters in the BW formalism implicitly absorb loop contributions, they cannot simulate nonsmooth behavior such as a TS. Thus, it is highly desirable to develop an appropriate approach where the data are fitted with a unitary

coupled-channel J/ψ decay amplitude, and $\eta(1405/1475)$ poles are searched by analytically continuing the amplitude. The $\eta(1405/1475)$ exists in a complicated coupled-channel system consisting of quasi-two-body channels such as $K^*\bar{K}$ and $a_0\pi$ and three-body channels such as $K\bar{K}\pi$ and $\pi\pi\eta$. The unitary coupled-channel approach seems the only possible option to describe such a system. Also in this approach, we automatically take account of the TS effects that are expected to play an important role, and thus taking over the sound physics in the previous models of Refs. [25–28].

In this work,¹ we develop a three-body unitary coupled-channel model for radiative J/ψ decays to three-meson final states of any J^{PC} . Then, we use the model to fit $K_S K_S \pi^0$ Dalitz plot pseudodata generated from the BESIII 0^{-+} amplitude for $J/\psi \rightarrow \gamma(K_S K_S \pi^0)$ [29]. At the same time, the branching fractions of other final states such as $\eta\pi^+\pi^-$ and $\rho^0\gamma$ relative to that of $K\bar{K}\pi$ are also fitted. Based on the obtained model, we examine the pole structure of $\eta(1405/1475)$ in the complex energy plane to see if $\eta(1405/1475)$ is one or two states. We also use the model to predict $\eta(1405/1475) \rightarrow \eta\pi\pi$, $\gamma\pi\pi$, and $\pi\pi\pi$ lineshapes and branchings. By examining the $\eta(1405/1475)$ decay mechanisms for different final states, we identify dominant mechanisms and address major issues regarding $\eta(1405/1475)$ how the process-dependent lineshapes and large isospin violations come about.

Precise Dalitz plot data are a great target for a three-body unitary model. Single-channel three-body unitary frameworks based on the Khuri-Treiman equations have been used extensively to analyze Dalitz data in elastic kinematical regions: e.g., Refs. [32,33] for $\omega/\phi \rightarrow \pi\pi\pi$. However, Dalitz-plot analyses covering inelastic kinematical regions with coupled-channel three-body unitary frameworks are very limited: e.g., Ref. [34] for $D^+ \rightarrow K^-\pi^+\pi^+$ and the present analysis. Since more and more precise Dalitz data are expected from the contemporary experimental facilities, the importance of the three-body unitary coupled-channel analysis will increase. Thus, related theoretical developments have been made recently [35–37].

A three-body unitary analysis like the present work involves pole extractions. Some works [38–40] have discussed the pole extraction from three-body unitarity amplitudes. Practically, however, such a pole extraction from experimental three-body distributions had not been done until recently. The first case was made in Refs. [41,42] where a $\rho\pi$ single-channel model was used to analyze $m_{\pi^+\pi^-\pi^-}$ lineshape data for $\tau^- \rightarrow \pi^+\pi^-\pi^-\nu_\tau$, extracting an $a_1(1260)$ pole. Reference [42] ([41]) treated the three-body unitarity rigorously (partially). The two analyses highlighted the importance of the full three-body unitarity in the pole extraction since an additional spurious pole existed in Ref. [41]. Our present analysis treats the three-body

¹A part of the results has been published in Ref. [31].

unitarity as rigorously as in Ref. [42]. Furthermore, we improve the pole extraction method of Ref. [42] since we consider relevant coupled channels and fit Dalitz plot distributions rather than the projected invariant mass distributions.

The organization of this paper is as follows. In Sec. II we present formulas for the radiative J/ψ decay amplitude based on the three-body unitary coupled-channel model and the partial decay width. In Sec. III we analyze Dalitz plot pseudodata from the BESIII 0^{-+} amplitude for $J/\psi \rightarrow \gamma(K_S K_S \pi^0)$. The quality of the fits is shown and the $\eta(1405/1475)$ poles are extracted. In Sec. IV we predict the lineshapes of $\eta\pi\pi$, $\gamma\pi^+\pi^-$, $\pi\pi\pi$ final states from the radiative J/ψ decays. The branching fractions for the $\pi\pi\pi$ final states are also predicted. Finally, in Sec. V we summarize the paper and discuss the future prospects.

II. MODEL

A. Radiative J/ψ decay amplitudes within a three-body unitary coupled-channel approach

In constructing our three-body unitary coupled-channel model, we basically follow the formulation presented in Refs. [34,35]. However, there is one noteworthy difference.

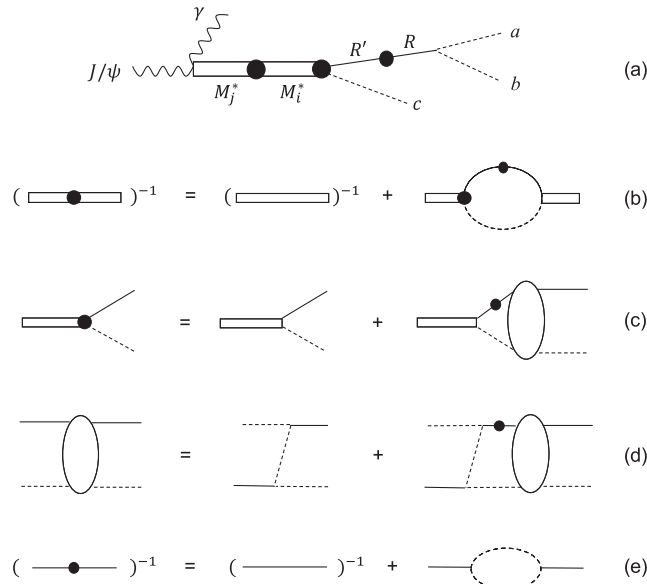


FIG. 1. (a) Diagrammatic representation for the radiative J/ψ decay amplitude of Eq. (2). The dashed lines represent pseudoscalar mesons, while the solid lines are bare two-meson resonances R . The double lines with $M_{i(j)}^*$ represent bare states for M^* such as $\eta(1405/1475)$. (b) Dressed M^* propagator: the first (second) diagram on the rhs is a bare M^* propagator (self-energy). (c) Dressed M^* decay vertex: the first (second) diagram is a bare vertex (rescattering term). The ellipse stands for the scattering amplitude X . (d) Lippmann-Schwinger-like equation for the amplitude X . (e) Dressed R propagator: the first (second) diagram is a bare R propagator (self-energy).

While we specified a particle with its isospin state in Refs. [34,35], we now use its charge state. This is an important extension of the model to describe isospin-violating processes. In what follows, we sketch our model, putting an emphasis on the differences from Refs. [34,35].

A radiative J/ψ decay mechanism within our model is diagrammatically represented by Fig. 1(a). First, J/ψ radiatively couples, via a vertex $\Gamma_{\gamma M_j^*, J/\psi}$, to a bare excited state (M^*) such as $\eta(1405/1475)$ of $J^{PC} = 0^{-+}$ and $f_1(1420)$ of $J^{PC} = 1^{++}$; we consider M^* with $I = 0$ (I : isospin) in this work. Second, the bare M^* nonperturbatively couples with quasi-two-body Rc and three-body abc states to form a dressed M^* propagator \bar{G}_{M^*} [Fig. 1(b)] that includes M^* resonance pole(s). Here, abc are pseudoscalar mesons (π, K, η) and R is a bare two-meson resonance such as K^* , $a_0(980)$, or $f_0(980)$. The particles R and ab also nonperturbatively couple through a vertex $\Gamma_{ab,R}$, forming a dressed R propagator $\tau_{R,R'}$ [Fig. 1(e)] that includes R resonance poles. Third, M^* decays to a final abc via a dressed $M_i^* \rightarrow Rc$ decay vertex $\bar{\Gamma}_{cR, M_i^*}$ [Fig. 1(c)] that includes nonperturbative final-state interactions. The amplitude formula for the above radiative J/ψ decay process is given by²

$$A_{\gamma abc, J/\psi} = \sum_{J^{PC}} A_{\gamma abc, J/\psi}^{J^{PC}}, \quad (1)$$

with

$$A_{\gamma abc, J/\psi}^{J^{PC}} = \sum_{abc}^{\text{cyclic}} \sum_{RR's_R^z} \sum_{ijs_{M^*}^z} \Gamma_{ab,R} \tau_{R,R'}(p_c, E - E_c) \times \bar{\Gamma}_{cR, M_i^*}(p_c, E) [\bar{G}_{M^*}(E)]_{ij} \Gamma_{\gamma M_j^*, J/\psi}, \quad (2)$$

where cyclic permutations $(abc), (cab), (bca)$ are indicated by $\sum_{abc}^{\text{cyclic}}$, the indices i and j specify one of the bare M^* states belonging to the same J^{PC} , and E denotes the abc total energy in the abc center-of-mass (CM) frame. Below, we give a more detailed expression for each of the components in the amplitude.

The $J/\psi \rightarrow \gamma M_j^*$ vertex is given in a general form as

$$\Gamma_{\gamma M_j^*, J/\psi} = \sum_{\ell \tilde{\ell}^z s} \frac{g_{J/\psi M_j^* \gamma}^{\ell s} (s_{M^*} \tilde{s}_{M^*}^z 1 \tilde{s}_\gamma^z |s \tilde{s}_{M^*}^z + \tilde{s}_\gamma^z)}{\sqrt{8 \tilde{E}_\gamma m_{J/\psi} m_{M_j^*}}} \times (\ell \tilde{\ell}^z s \tilde{s}_{M^*}^z + \tilde{s}_\gamma^z |1 \tilde{s}_\gamma^z) Y_{\ell \tilde{\ell}^z}(\hat{p}_\gamma) \tilde{P}_\gamma^\ell, \quad (3)$$

²We denote a particle x 's mass, momentum, energy, polarization, spin and z component in the abc CM frame by $m_x, p_x, E_x, \epsilon_x, s_x$, and s_x^z , respectively; $E_x = \sqrt{m_x^2 + p_x^2}$ with $p_x = |\mathbf{p}_x|$. The mass values for pseudoscalar mesons (π, K, η) are taken from Ref. [15]. Symbols with a tilde such as \tilde{p}_x indicate quantities in the J/ψ -at-rest frame.

where $g_{J/\psi M_i^* \gamma}^{\ell s}$ is a coupling constant and $m_{M_i^*}$ is a bare M_i^* mass, $Y_{\ell m}(\hat{q})$ denotes the spherical harmonics with $\hat{q} \equiv \mathbf{q}/|\mathbf{q}|$, and \sum_{ℓ} is restricted by parity conservation. When M^* belongs to $J^{PC} = 0^{-+}$, Eq. (3) reduces to (up to a constant overall factor)

$$\Gamma_{\gamma_{J/\psi}^* J/\psi} = \frac{g_{J/\psi M_i^* \gamma} (\tilde{\boldsymbol{\epsilon}}_{J/\psi} \times \tilde{\boldsymbol{\epsilon}}_{\gamma}) \cdot \tilde{\boldsymbol{p}}_{\gamma}}{\sqrt{8\tilde{E}_{\gamma} m_{J/\psi} m_{M_i^*}}}. \quad (4)$$

In our numerical analysis from Sec. III, we use the coupling $g_{J/\psi M_i^* \gamma}$ defined in this reduced form. The $R \rightarrow ab$ vertex is given by

$$\begin{aligned} \Gamma_{ab,R} &= (t_a t_a^z t_b t_b^z | t_R t_R^z) \sum_{LL^z SS^z} (s_a s_a^z s_b s_b^z | SS^z) \\ &\times (LL^z SS^z | s_R s_R^z) Y_{LL^z}(\hat{p}_a^*) \\ &\times \sqrt{\frac{m_R E_a(p_a^*) E_b(p_b^*)}{E_R(p_c) E_a(p_a) E_b(p_b)}} f_{ab,R}^{LS}(p_a^*), \quad (5) \end{aligned}$$

where the parentheses are Clebsch-Gordan coefficients, t_x and t_x^z are the isospin of a particle x and its z component, respectively, and \mathbf{p}_a^* denotes a particle a 's momentum in the ab CM frame. Since particles a and b are pseudoscalars in this paper, the total spin is $S = 0$ and the orbital angular momentum is $L = s_R$. Thus, we simplify the above notation for the $R \rightarrow ab$ vertex as

$$\begin{aligned} \Gamma_{ab,R} &= (t_a t_a^z t_b t_b^z | t_R t_R^z) Y_{s_R, s_R^z}(\hat{p}_a^*) \\ &\times \sqrt{\frac{m_R E_a(p_a^*) E_b(p_b^*)}{E_R(p_c) E_a(p_a) E_b(p_b)}} f_{ab,R}(p_a^*), \quad (6) \end{aligned}$$

with a vertex function

$$f_{ab,R}(q) = g_{ab,R} \frac{(1 + q^2/c_{ab,R}^2)^{-\frac{1}{2}} q^L}{\sqrt{m_R E_a(q) E_b(q)} m_{\pi}^{L-1}}, \quad (7)$$

and use this notation hereafter. The coupling $g_{ab,R}$ and cutoff $c_{ab,R}$ in Eq. (7) and the bare mass m_R in Eq. (8) are determined by analyzing L -wave ab scattering data as detailed in Appendix A where the parameter values are presented.

The dressed R propagator [Fig. 1(e)] is given by

$$[\tau^{-1}(p, E)]_{R,R'} = [E - E_R(p)] \delta_{R,R'} - \Sigma_{R,R'}(p, E), \quad (8)$$

with the R self-energy

$$\begin{aligned} \Sigma_{R,R'}(p, E) &= \sum_{ab} (t_a t_a^z t_b t_b^z | t_R, t_a^z + t_b^z) (t_a t_a^z t_b t_b^z | t_{R'}, t_a^z + t_b^z) \\ &\times \sqrt{\frac{m_R m_{R'}}{E_R(p) E_{R'}(p)}} \int q^2 dq \frac{M_{ab}(q)}{\sqrt{M_{ab}^2(q) + p^2}} \\ &\times \frac{\mathcal{B}_{ab} f_{R,ab}(q) f_{ab,R'}(q)}{E - \sqrt{M_{ab}^2(q) + p^2} + ic}, \quad (9) \end{aligned}$$

where $M_{ab}(q) = E_a(q) + E_b(q)$ and m_R is the bare mass of R ; R and R' in Eq. (9) have the same spin state ($s_R = s_{R'}$). Due to Bose symmetry, we have a factor \mathcal{B}_{ab} : $\mathcal{B}_{ab} = 1/2$ for identical particles a and b , and $\mathcal{B}_{ab} = 1$ otherwise. In Eq. (9), the a_0 - f_0 mixing occurs ($\Sigma_{a_0, f_0} \neq 0$) due to the mass difference between $ab = K^+ K^-$ and $K^0 \bar{K}^0$ states. The dressed R propagators include R resonance poles, as summarized in Tables III–V in Appendix A.

The dressed $M_i^* \rightarrow Rc$ decay vertex [Fig. 1(c)] is given by

$$\begin{aligned} \bar{\Gamma}_{cR, M_i^*}(p_c, E) &= \sum_{l, l^z} (ll^z s_R s_R^z | s_{M_i^*} s_{M_i^*}^z) (t_R t_R^z t_c t_c^z | t_{M_i^*} t_{M_i^*}^z) \\ &\times Y_{l, l^z}(-\hat{p}_c) \bar{F}_{(cR)_l, M_i^*}(p_c, E), \quad (10) \end{aligned}$$

where l is the relative orbital angular momentum between R and c . The dressed $M_i^* \rightarrow Rc$ vertex function is

$$\begin{aligned} \bar{F}_{(cR)_l, M_i^*}(p_c, E) &= F_{(cR)_l, M_i^*}(p_c) + \sum_{c'R'R'l'} \int q^2 dq \\ &\times X_{(cR)_l, (c'R')_l}^{J^{PC}}(p_c, q; E) \\ &\times \tau_{R', R'}(q, E - E_{c'}) F_{(c'R')_l, M_i^*}(q), \quad (11) \end{aligned}$$

where the first and second terms are direct decay and rescattering mechanisms, respectively. Common isobar models do not have the second term. We use a bare vertex function including a dipole form factor as

$$F_{(cR)_l, M_i^*}(q) = C_{(cR)_l}^{M_i^*} \frac{[1 + q^2/(\Lambda_{(cR)_l}^{M_i^*})^2]^{-2-\frac{1}{2}} q^l}{\sqrt{8E_c(q) E_R(q) m_{M_i^*}} m_{\pi}^{l-1}}, \quad (12)$$

where $C_{(cR)_l}^{M_i^*}$ and $\Lambda_{(cR)_l}^{M_i^*}$ are coupling and cutoff parameters, respectively. We also introduced J^{PC} partial-wave amplitudes for $cR \rightarrow c'R'$ scatterings, $X_{(cR)_l, (c'R')_l}^{J^{PC}}$, that are obtained by solving the scattering equation [Fig. 1(d)]:

$$\begin{aligned}
& X_{(c'R')_{\rho'},(cR)_l}^{JPC}(p', p; E) \\
&= V_{(c'R')_{\rho'},(cR)_l}^{JPC}(p', p; E) \\
&+ \sum_{c'', R'', R''', l''} \int q^2 dq V_{(c'R')_{\rho'},(c''R''')_{\rho''}}^{JPC}(p', q; E) \\
&\times \tau_{R'', R'''}(q, E - E_{c''}) X_{(c''R''')_{\rho''},(cR)_l}^{JPC}(q, p; E), \quad (13)
\end{aligned}$$

with

$$\begin{aligned}
V_{(c'R')_{\rho'},(cR)_l}^{JPC}(p', p; E) &= Z_{(c'R')_{\rho'},(cR)_l}^{\bar{c}, JPC}(p', p; E) \\
&+ v_{(c'R')_{\rho'},(cR)_l}^{\text{HLS}, JPC}(p', p). \quad (14)
\end{aligned}$$

The driving term $Z_{(c'R')_{\rho'},(cR)_l}^{\bar{c}, JPC}$, which we call the Z diagram, is diagrammatically expressed in the first term on the rhs of Fig. 1(d); \bar{c} indicates an exchanged particle. Explicit formulas for the partial-wave-expanded Z diagram can be found in Appendix C of Ref. [35]. One important difference from Ref. [35] is that here we do not project the Z diagrams onto a definite total isospin state. As a result, an isospin-violating $K^* \bar{K} \rightarrow f_0 \pi$ process is caused by a Z diagram and $m_{K^\pm} \neq m_{K^0}$, leading to $\eta^* \rightarrow \pi\pi$.

The second term on the rhs of Eq. (14) is a vector-meson exchange mechanism based on the hidden local symmetry model [43]. In the present case, this mechanism works for $K^* \bar{K} \leftrightarrow K^* \bar{K}, \bar{K}^* K$ interactions. Formulas were presented in Appendix A of Ref. [34], but here we use a different form factor of $(1 + p^2/\Lambda^2)^{-2}(1 + p'^2/\Lambda^2)^{-2}$ with $\Lambda = 1$ GeV, rather than Eq. (A15) of Ref. [34].

The dressed M^* propagator [Fig. 1(b)] is given by

$$[\bar{G}_{M^*}^{-1}(E)]_{ij} = (E - m_{M_i^*})\delta_{ij} - [\Sigma_{M^*}(E)]_{ij}, \quad (15)$$

where the M^* self-energy in the second term is given by

$$\begin{aligned}
[\Sigma_{M^*}(E)]_{ij} &= \mathcal{B}_{Rc} \sum_{cRR'l} \int q^2 dq F_{(cR)_l, M_i^*}(q) \\
&\times \tau_{R, R'}(q, E - E_c(q)) \bar{F}_{(cR')_l, M_j^*}(q, E). \quad (16)
\end{aligned}$$

The above formulas show that the dressed M^* propagator (M^* pole structure) and the dressed $M_i^* \rightarrow Rc$ form factor (M^* decay mechanism) are explicitly related by the common dynamics. This is a consequence of the three-body unitarity.

In the above formulas, we assumed that two-body $ab \rightarrow a'b'$ interactions occur via bare R excitations, $ab \rightarrow R \rightarrow a'b'$. We can straightforwardly extend the formulas if two-body interactions are from bare R excitations and separable contact interactions, as detailed in Ref. [34]. Also, the above formulas are valid when c is a pseudoscalar meson, and they need to be slightly modified for the $Rc = \rho\rho$ channel. We consider the spectator ρ width in the first

term on the rhs of Eq. (8) by $E - E_R(p) \rightarrow E - E_R(p) + i\Gamma_\rho/2$; $\Gamma_\rho = 150$ MeV and is constant. Also, the label in the bare form factor of Eq. (12) is extended to include the total spin of $\rho\rho$ ($s_{\rho\rho}$) as $(cR)_l \rightarrow (cR)_{ls_{\rho\rho}}$.

For describing $J/\psi \rightarrow \gamma M^* \rightarrow \gamma(\gamma\pi^+\pi^-)$, we assume the vector-meson-dominance mechanism where the $\rho\rho$ channel from $M_i^* \rightarrow \rho\rho$ or coupled-channel dynamics is followed by $\rho \rightarrow \gamma$ and $\rho \rightarrow \pi^+\pi^-$. The photon- ρ direct coupling is from the vector-meson-dominance model. This mechanism can be implemented in the decay amplitude formula of Eq. (2) by multiplying by $2e/g_\rho$; each of the two ρ 's can couple to the photon, giving a factor of 2, and $e^2/4\pi \simeq 1/137$ and $g_\rho^2/4\pi = 2.2$. There are some experimental indications for $\eta(1405/1475) \rightarrow \rho\rho \rightarrow 4\pi$ but they are rather uncertain [2,44]. Thus, we do not calculate this process in this paper.

B. Radiative J/ψ decay rate formula

The partial decay width for a radiative J/ψ decay, $J/\psi \rightarrow \gamma(abc)$, is given by

$$\begin{aligned}
d\Gamma_{J/\psi \rightarrow \gamma(abc)} &= \frac{\mathcal{B}}{2^5 (2\pi)^8 m_{J/\psi}} |\mathcal{M}_{J/\psi \rightarrow \gamma(abc)}|^2 \delta^{(4)}(p_i - p_f) \\
&\times \frac{d^3 p_a}{E_a} \frac{d^3 p_b}{E_b} \frac{d^3 p_c}{E_c} \frac{d^3 p_\gamma}{E_\gamma} \\
&= \frac{\mathcal{B}}{(2\pi)^5} \frac{\tilde{p}_\gamma^2}{\tilde{E}_\gamma} \frac{|\mathcal{M}_{J/\psi \rightarrow \gamma(abc)}|^2}{32 m_{J/\psi} E^2} d\tilde{p}_\gamma dm_{ab}^2 dm_{ac}^2, \quad (17)
\end{aligned}$$

where m_{ab} and m_{ac} are the invariant masses of the ab and ac subsystems, respectively, \tilde{p}_γ denotes the photon momentum in the J/ψ -at-rest frame, and $\mathcal{M}_{J/\psi \rightarrow \gamma(abc)}$ is the invariant amplitude that is related to Eq. (1) with an overall kinematical factor. The Bose factor \mathcal{B} is $\mathcal{B} = 1/3!$ for three identical particles abc , $\mathcal{B} = 1/2!$ for two identical particles among abc , and $\mathcal{B} = 1$ otherwise. The J/ψ spin state is implicitly averaged.

Using our amplitude in Eq. (2) for the J/ψ radiative decays via M^* excitations, the decay formula of Eq. (17) can be written as

$$\frac{d\Gamma_{J/\psi \rightarrow \gamma(abc)}}{dE} = \sum_{JPC} \frac{d\Gamma_{J/\psi \rightarrow \gamma(abc)}^{JPC}}{dE}, \quad (18)$$

with

$$\begin{aligned}
\frac{d\Gamma_{J/\psi \rightarrow \gamma(abc)}^{JPC}}{dE} &= \frac{2E^2}{\pi} \sum_{ijs_{M^*}^z} \sum_{k\ell s_{M^*}^z} d\Gamma_{M^* \rightarrow abc}^{ik} \frac{[\bar{G}_{M^*}(E)]_{ij}}{\sqrt{m_{M_i^*} m_{M_j^*}}} \\
&\times \frac{[\bar{G}_{M^*}(E)]_{k\ell}^*}{\sqrt{m_{M_k^*} m_{M_\ell^*}}} \Gamma_{J/\psi \rightarrow M^* \gamma}^{j\ell}, \quad (19)
\end{aligned}$$

where $s_{M^*}^z$ ($s_{M^*}^{Iz}$) is a spin state of M^* in \tilde{G}_{M^*} ($[\tilde{G}_{M^*}]^*$), and

$$d\Gamma_{M^* \rightarrow abc}^{ij} \equiv \mathcal{B} \frac{\mathcal{M}_{M_i^* \rightarrow abc} \mathcal{M}_{M_j^* \rightarrow abc}}{(2\pi)^3 32E^3} dm_{ab}^2 dm_{ac}^2, \quad (20)$$

$$\Gamma_{J/\psi \rightarrow M^* \gamma}^{ij} \equiv \frac{1}{8\pi} \frac{\tilde{P}_\gamma}{m_{J/\psi}^2} \mathcal{M}_{J/\psi \rightarrow M_i^* \gamma} \mathcal{M}_{J/\psi \rightarrow M_j^* \gamma}^*. \quad (21)$$

The invariant amplitudes $\mathcal{M}_{M_i^* \rightarrow abc}$ and $\mathcal{M}_{J/\psi \rightarrow M_i^* \gamma}$ are related to components of the amplitude in Eq. (2) by

$$\mathcal{M}_{M_i^* \rightarrow abc} = -(2\pi)^3 \sqrt{16m_{M_i^*} E_a E_b E_c} T_{M_i^* \rightarrow abc}, \quad (22)$$

with

$$T_{M_i^* \rightarrow abc} = \sum_{abc}^{\text{cyclic}} \sum_{RR's_R^z} \Gamma_{ab,R\tau_{R,R'}}(p_c, E - E_c) \times \bar{\Gamma}_{cR',M_i^*}(\mathbf{p}_c, E), \quad (23)$$

and

$$\mathcal{M}_{J/\psi \rightarrow M_i^* \gamma} = \sqrt{8\tilde{E}_\gamma m_{J/\psi} m_{M_i^*}} \Gamma_{\gamma M_i^*, J/\psi}. \quad (24)$$

For the case of $i = j$, Eqs. (20) and (21) reduce to the standard formulas of the M^* -decay Dalitz plot distribution and J/ψ two-body decay width, respectively. Our decay formula in Eq. (19) can be made look similar to that of a Breit-Wigner model by the replacement $[\tilde{G}_{M^*}(E)]_{ij} \rightarrow \delta_{ij}/(E - M_{M_i^*} + i\Gamma_{M_i^*}/2)$, with $M_{M_i^*}$ and $\Gamma_{M_i^*}$ being the Breit-Wigner mass and width, respectively.

III. DATA ANALYSIS AND $\eta(1405/1475)$ POLES

In this paper, we study radiative J/ψ decays via $\eta(1405/1475)$ excitations with the unitary coupled-channel model described above. We thus consider only the $J^{PC} = 0^{-+}$ partial-wave contribution in the above formulas. In the following, we discuss our data set, our default setup of the model, and analysis results.

A. Data set

A main part of our data set is $K_S K_S \pi^0$ Dalitz plot pseudodata. We generate the pseudodata using the E -dependent 0^{-+} partial-wave amplitude from the recent BESIII Monte Carlo (MC) analysis on $J/\psi \rightarrow \gamma(K_S K_S \pi^0)$ [29]. We often denote this process by $J/\psi \rightarrow \gamma(0^{-+}) \rightarrow \gamma(K_S K_S \pi^0)$. The pseudodata is therefore detection-efficiency-corrected and background free.

The pseudodata includes $\sim 1.23 \times 10^5$ events in total, being consistent with the BESIII data, and is binned as follows. The range of $1300 \leq E \leq 1600$ MeV is divided into 30 E bins (10 MeV bin width, labeled by l).

Furthermore, in each E bin, we equally divide $(0.95 \text{ GeV})^2 \leq m_{K_S K_S}^2 \leq (1.50 \text{ GeV})^2$ and $(0.60 \text{ GeV})^2 \leq m_{K_S \pi^0}^2 \leq (1.15 \text{ GeV})^2$ into 50×50 bins (labeled by m); m_{ab} is the ab invariant mass. We denote the event numbers in the $\{l, m\}$ and l th bins by $N_{l,m}$ and $\bar{N}_l (\equiv \sum_m N_{l,m})$, respectively; their statistical uncertainties are $\sqrt{N_{l,m}}$ and $\sqrt{\bar{N}_l}$, respectively. We fit both $\{N_{l,m}\}$ and $\{\bar{N}_l\}$ pseudodata, since $\{N_{l,m}\}$ and $\{\bar{N}_l\}$ would efficiently constrain the detailed decay dynamics and the resonant behavior (pole structure) of $\eta(1405/1475)$, respectively. We use the bootstrap method [45] to estimate the statistical uncertainty of the model, and we thus generate and fit 50 pseudodata samples.

Other final states from the radiative J/ψ decays are also considered in our analysis. We fit the model to a ratio of partial decay widths [15],

$$R_1^{\text{exp}} = \frac{\Gamma[J/\psi \rightarrow \gamma \eta(1405/1475) \rightarrow \gamma(K\bar{K}\pi)]}{\Gamma[J/\psi \rightarrow \gamma \eta(1405/1475) \rightarrow \gamma(\eta\pi^+\pi^-)} = \frac{(2.8 \pm 0.6) \times 10^{-3}}{(3.0 \pm 0.5) \times 10^{-4}} = 6.8 - 11.9, \quad (25)$$

and also another ratio [8,9],

$$R_2^{\text{exp}} = \frac{\Gamma[J/\psi \rightarrow \gamma \eta(1405/1475) \rightarrow \gamma(\rho^0 \gamma)]}{\Gamma[J/\psi \rightarrow \gamma \eta(1405/1475) \rightarrow \gamma(K\bar{K}\pi)]} = 0.015 - 0.043. \quad (26)$$

The partial widths Γ in the above ratios are calculated by integrating the E distributions [Eq. (18)] for $K\bar{K}\pi$, $\pi^+\pi^-\eta$, and $\rho^0\gamma$ final states over the range of $1350 \text{ MeV} < E < 1550 \text{ MeV}$. The ratio of Eq. (25) is important to constrain the $a_0(980)\pi$ contributions since the relative coupling strengths of $a_0(980) \rightarrow K\bar{K}$ and $a_0(980) \rightarrow \eta\pi$ are experimentally fixed in a certain range [46–49]. Also, $f_0\eta$ and $\rho\rho$ channels indirectly contribute to $K_S K_S \pi^0$ through loops, and therefore the $K_S K_S \pi^0$ data does not constrain their parameters well. Since these channels directly contribute to the $\eta\pi^+\pi^-$ and $\rho^0\gamma$ final states, the above ratios will be a good constraint. The partial width for all $K\bar{K}\pi$ final states in Eqs. (25) and (26) is 12 times larger than that of $K_S K_S \pi^0$, as determined by the isospin Clebsch-Gordan coefficients.

The MC-solution-based $\{N_{l,m}\}$, $\{\bar{N}_l\}$, R_1^{exp} , and R_2^{exp} are simultaneously fitted, with a χ^2 minimization, by our default model described in the next subsection; the actual BESIII data are not directly fitted. We calculate χ^2 from $\{N_{l,m}\}$ by comparing $N_{l,m}$ to the differential decay width $[d\Gamma_{J/\psi \rightarrow \gamma(abc)}/dEdm_{ab}^2 dm_{ac}^2]$ in Eqs. (18)–(21) evaluated at the bin center and multiplied by the bin volume. We omit $N_{l,m}$ on the phase-space boundary from the χ^2 calculation. This simplified procedure keeps the computation time reasonable. Also, if a bin has $N_{l,m} < 10$, it is combined

with neighboring bins to have more than nine events for the χ^2 calculation. The number of bins for $\{N_{l,m}\}$ depends on the pseudodata samples, and is 4496–4575. χ^2 's from $\{\bar{N}_l\}$, R_1^{exp} , and R_2^{exp} are weighted appropriately to reasonably constrain the model.

B. Model setup

For the present analysis of the radiative J/ψ decays, we consider the following coupled channels as a default in our model described in Sec. II. We include two bare M^* of $J^{PC} = 0^{-+}$; we refer to them as η^* hereafter. The Rc channels are $Rc = K^*(892)\bar{K}$, $\kappa\bar{K}$, $a_0(980)\pi$, $a_2(1320)\pi$, $f_0\eta$, $\rho(770)\rho(770)$, and $f_0\pi$, where charge indices are suppressed.³ To form positive C -parity states, $\bar{K}^*(892)K$ and $\bar{\kappa}K$ channels are implicitly included. A symbol R may refer to more than one bare state and/or contact interaction. For example, the $f_0\pi$ channel includes two bare states and one contact interaction that nonperturbatively couple with $\pi\pi - K\bar{K}$ continuum states, forming $f_0(500)$, $f_0(980)$, and $f_0(1370)$ poles; see Appendix A for details.

Regarding the $\pi\eta - K\bar{K}$ coupled-channel s -wave scattering amplitude that includes an $a_0(980)$ pole, we consider two experimental inputs; see Appendix A 2 for details. First, the $a_0(980)$ amplitude from the BESIII amplitude analysis on $\chi_{c1} \rightarrow \eta\pi^+\pi^-$ constrains the energy dependence of our $a_0(980)$ model. Second, we determine $a_0(980) \rightarrow K\bar{K}$ and $a_0(980) \rightarrow \eta\pi$ decay strengths using an analysis of $p\bar{p} \rightarrow K\bar{K}\pi, \eta\pi\pi$ [46] giving $|g_{a_0(980) \rightarrow K\bar{K}}/g_{a_0(980) \rightarrow \eta\pi}| \sim 1$; $g_{a_0(980) \rightarrow ab}$ is the residue of $a_0(980) \rightarrow ab$ decay. The ratio of branching fractions of $a_0(980) \rightarrow K\bar{K}$ and $a_0(980) \rightarrow \eta\pi$, which can be translated into $|g_{a_0(980) \rightarrow K\bar{K}}/g_{a_0(980) \rightarrow \eta\pi}|$, has not been precisely determined experimentally [15,46–49]. Later, we will discuss possible impacts of using a different $a_0(980)$ model with different $|g_{a_0(980) \rightarrow K\bar{K}}/g_{a_0(980) \rightarrow \eta\pi}|$.

We mention the channels considered in the BESIII amplitude analysis of $J/\psi \rightarrow \gamma(K_S K_S \pi^0)$ [29]. In the 0^{-+} partial wave, the BESIII Collaboration considered $\eta(1405)$ and $\eta(1475)$ resonances that decay into $K^*(892)\bar{K}$, $a_0(980)\pi$, and $a_2(1320)\pi$. All resonances, except for $a_0(980)$, are described with Breit-Wigner amplitudes. No rescattering or channel coupling such as those in the second term on the rhs of Fig. 1(c) is taken into account. In addition, a nonresonant $K\pi p$ -wave amplitude supplements the $K^*(892)$ tail region. Clearly, our coupled-channel model includes more channels than the BESIII model does. This is to satisfy the coupled-channel three-body unitarity and describe different final states in a unified manner.

We consider isospin-conserving $\eta^* \rightarrow Rc$ decays in Eq. (12) for all bare η^* and Rc states specified in the first paragraph of this subsection. One exception applies to the lighter bare $\eta^* \rightarrow \rho\rho$, which is set to zero. This is because

the lighter bare η^* seems consistent with an excited $s\bar{s}$ state from the quark η model [16] and LQCD prediction [23], and $s\bar{s} \rightarrow \rho\rho$ should be small for the Okubo-Zweig-Iizuka rule.

We may add nonresonant (NR) amplitudes $A_{\gamma abc, J/\psi}^{J^{PC}, \text{NR}}$, which do not involve M^* excitations, to the resonant amplitudes $A_{\gamma abc, J/\psi}^{J^{PC}}$ of Eq. (1). We can derive $A_{\gamma abc, J/\psi}^{J^{PC}, \text{NR}}$ and modify $A_{\gamma abc, J/\psi}^{J^{PC}}$ so that their sum still maintains the three-body unitarity. However, this introduces too many fitting parameters to determine with the data set in the present analysis. We thus use a simplified NR amplitude in this work [cf. Eq. (4)]:

$$\mathcal{M}_{J/\psi \rightarrow \gamma(abc)}^{\text{NR}} = c_{\text{NR}}(\tilde{\epsilon}_{J/\psi} \times \tilde{\epsilon}_\gamma) \cdot \tilde{\mathbf{p}}_\gamma, \quad (27)$$

where c_{NR} is a complex constant. Only when fitting the $J/\psi \rightarrow \gamma(0^{-+}) \rightarrow \gamma K_S K_S \pi^0$ Dalitz plot pseudodata, this NR term is added to $\mathcal{M}_{J/\psi \rightarrow \gamma(abc)}$ in Eq. (17) and c_{NR} is determined by the fit.

We summarize the parameters fitted to the data set discussed in the previous subsection. We have two bare η^* masses in Eq. (15), two complex coupling constants ($g_{J/\psi \eta^* \gamma}$) in Eq. (4), and one complex constant c_{NR} in Eq. (27). We also adjust real coupling parameters $C_{(cR)_i}^{M_i^*}$ in Eq. (12). While the cutoffs $\Lambda_{(cR)_i}^{M_i^*}$ in Eq. (12) are also adjustable, we fix them to 700 MeV in this work to reduce the number of fitting parameters and speed up the fitting procedure. Since the overall strength and phase of the full amplitude are arbitrary, we have 25 fitting parameters in total. The parameter values obtained from the fit are presented in Table IX of Appendix B.

All of the radiative J/ψ decay processes included in our data set for the fit are isospin conserving. Since the isospin-violating effects are very small in these processes, we make the model isospin symmetric for fitting and extracting poles and thus use the averaged mass for each isospin multiplet. The amplitude formulas in Sec. II A reduce to the isospin-symmetric ones given in Refs. [34,35]. This simplification significantly speeds up the fitting and pole extraction procedures. When calculating the isospin-violating $J/\psi \rightarrow \gamma(0^{-+}) \rightarrow \gamma(\pi\pi\pi)$ amplitude of Eq. (2), we still use the isospin-symmetric $\tilde{G}_{\eta^*}(E)$ and parameters determined by fitting the data set, and the pole positions stay the same; the isospin violations occur in $\tau_{R,R'}$ and $\bar{\Gamma}_{cR, \eta_i^*}$ due to the difference between m_{K^\pm} and m_{K^0} .

C. Fits to $K_S K_S \pi^0$ Dalitz plot pseudodata generated from the BESIII 0^{-+} amplitude

By fitting the 50 bootstrap samples of the $K_S K_S \pi^0$ Dalitz plot pseudodata with the default dynamical contents described above, we obtain $\chi^2/\text{d.o.f.} = 1.40\text{--}1.54$ by comparing with $\{N_{l,m}\}$. The ratios of Eqs. (25) and (26) are also fitted simultaneously, obtaining $R_1^{\text{th}} \sim 7.5$ and $R_2^{\text{th}} \sim 0.025$, respectively.

³ κ is also referred to as $K_0^*(700)$ in the literature.

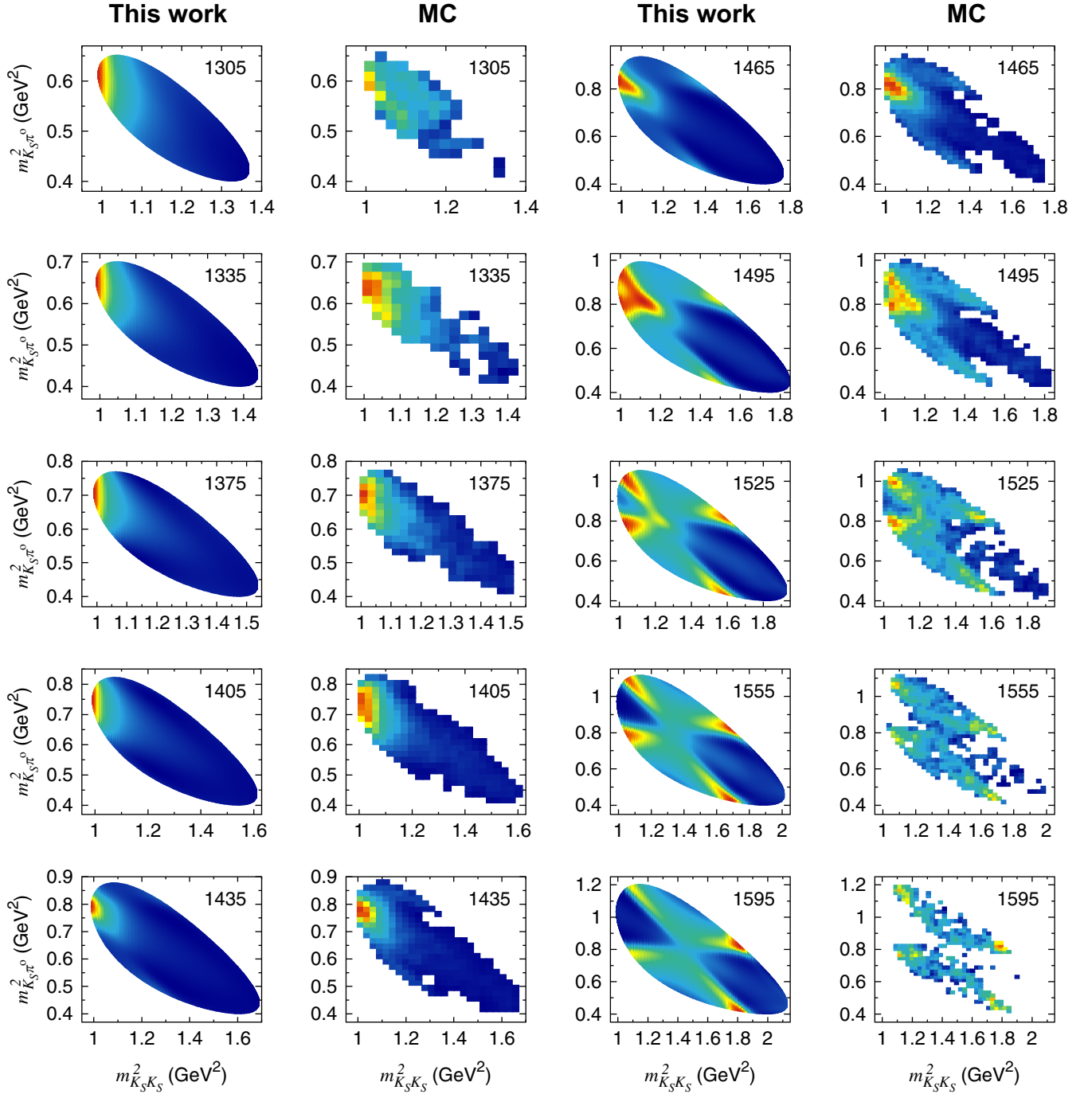


FIG. 2. $K_S K_S \pi^0$ Dalitz plot distributions for $J/\psi \rightarrow \gamma(0^{--}) \rightarrow \gamma(K_S K_S \pi^0)$. Our fit result and pseudodata (MC) are shown. The E values used in our calculation (the central values of the E bins of the pseudodata) are indicated in each panel. The distributions are shown, in descending order, in red, yellow, green, and blue. Depending on E , the same color means different absolute values.

The Dalitz plot distributions obtained from the fit are shown in Fig. 2 for representative E values, in comparison with one of the bootstrap samples.⁴ The fit quality is

⁴The same bootstrap sample is also shown in Figs. 3, 4, 5(a), 7, and 8.

reasonable overall. For $E \lesssim 1400$ MeV, there is a peak near the $K_S K_S$ threshold. While this is seemingly the $a_0(980)$ contribution, it is actually due to a constructive interference between $K^*(892)$ and $\bar{K}^*(892)$, as detailed later. For $E \gtrsim 1430$ MeV, on the other hand, the main pattern is mostly understood as the $K^*(892)$ and $\bar{K}^*(892)$ resonance contributions. The good fit quality can be seen more clearly

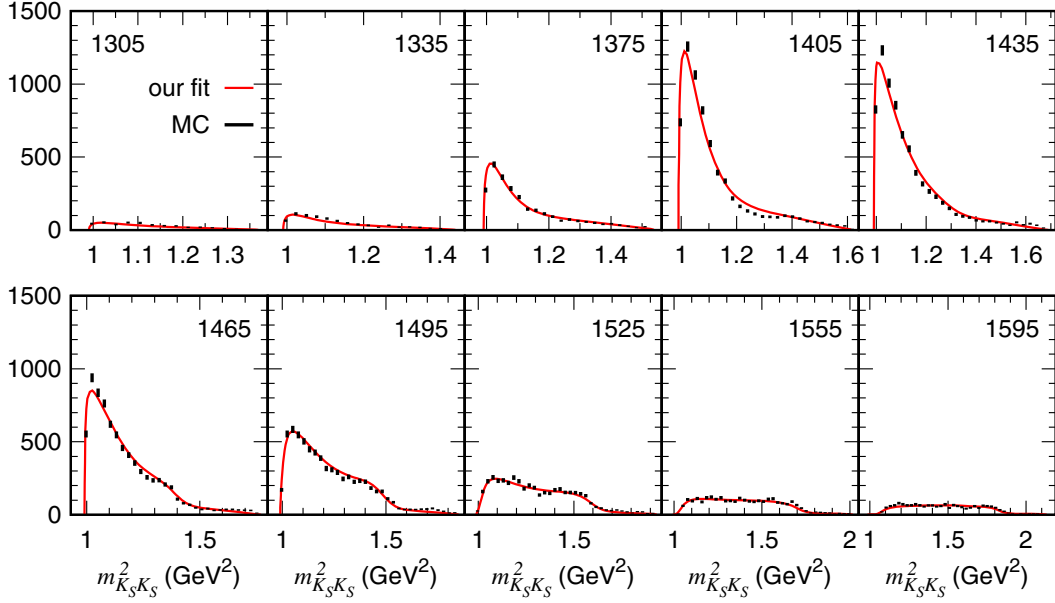


FIG. 3. $K_S K_S$ invariant mass distributions for $J/\psi \rightarrow \gamma(0^{-+}) \rightarrow \gamma(K_S K_S \pi^0)$. Our fit result (red solid curve) and the pseudodata (black error bars) are shown. The E values are indicated in each panel.

in the $K_S K_S$ and $K_S \pi^0$ invariant mass distributions, as shown in Figs. 3 and 4, respectively. The model is well fitted to the K^* peak (the sharp peak near the $K_S K_S$ threshold) in the $m_{K_S \pi^0}^2$ ($m_{K_S K_S}^2$) distributions.

The E dependence of the radiative J/ψ decay to $K_S K_S \pi^0$, obtained by integrating the Dalitz plots in Fig. 2, is shown in Fig. 5(a). The E dependence would be largely determined by the pole structure of the $\eta(1405/1475)$ resonances. The E distribution shows a broad peak with an almost flat top, and our model

reasonably agrees with the pseudodata. We now study dynamical details. The η^* decay mechanisms can be separated according to Rc states in Fig. 1(a) that directly couple to the final states. We will refer to these Rc states as *final Rc* states. Contributions from the final $K^* \bar{K}$, $\kappa \bar{K}$, and $a_0(980)\pi$ states are shown separately in Fig. 5(a). The final $K^* \bar{K}$ and $\kappa \bar{K}$ contributions are the first and second largest, while the final $a_0(980)\pi$ contribution is very small. The constant nonresonant contribution from Eq. (27) gives a small phase-space shape contribution.

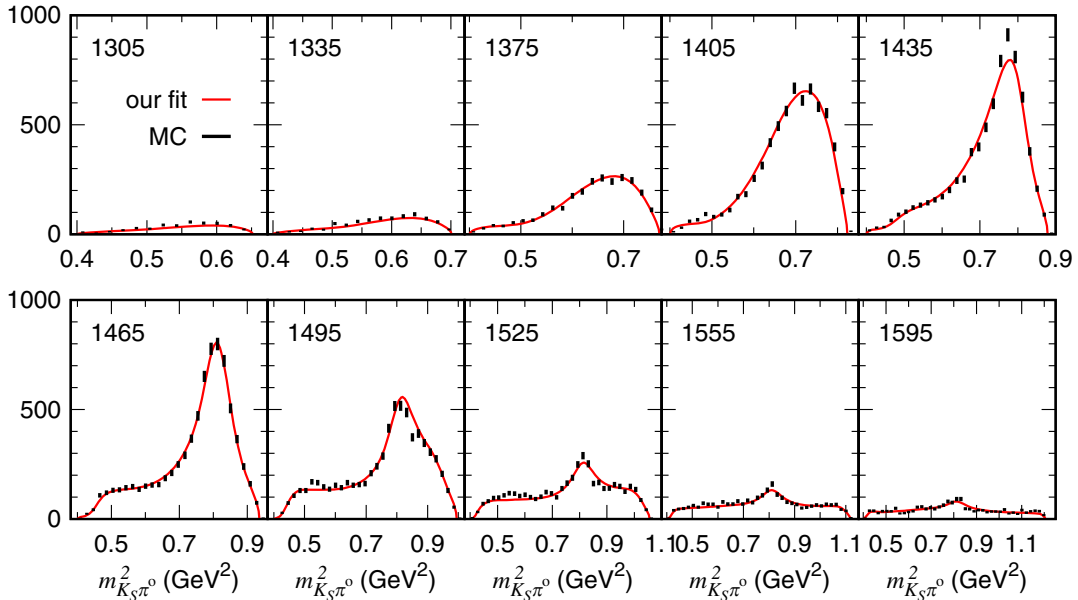


FIG. 4. $K_S \pi^0$ invariant mass distributions. Other features are the same as those in Fig. 3.

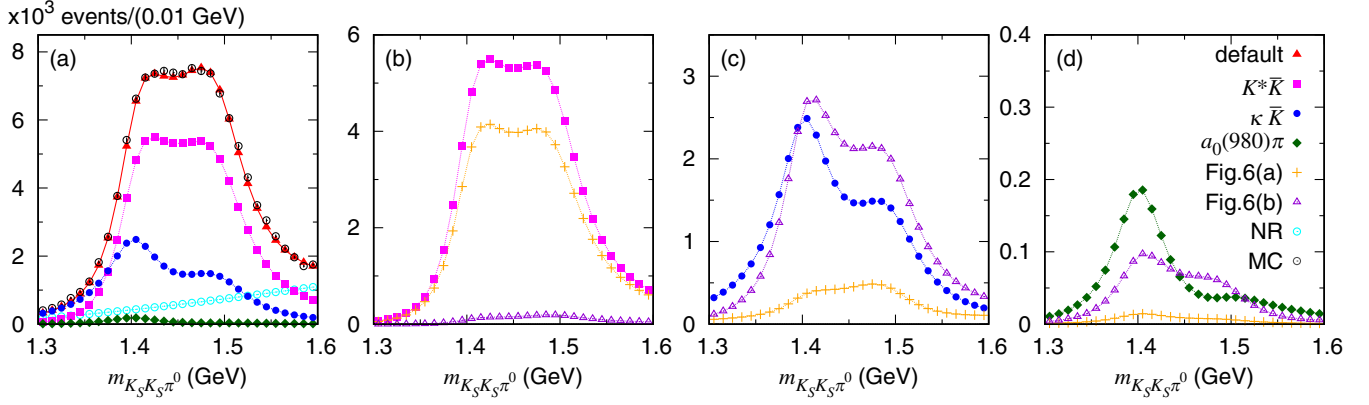


FIG. 5. $m_{K_S K_S \pi^0} (= E)$ distribution for $J/\psi \rightarrow \gamma(0^{++}) \rightarrow \gamma(K_S K_S \pi^0)$. (a) Our default fit to the pseudodata (MC). Final $K^* \bar{K}$, $\kappa \bar{K}$, and $a_0(980)\pi$ contributions as well as the NR contribution are also shown. (b) Final $K^* \bar{K}$ contribution. The main contributions from the diagrams of Figs. 6(a) and 6(b) are also shown. (c) [(d)] Final $\kappa \bar{K}$ [$a_0(980)\pi$] contribution, shown similarly to panel (b). Lines connecting the points are just to guide the eyes. Panel (a) is taken from Ref. [31].

The final $K^* \bar{K}$, $\kappa \bar{K}$, and $a_0(980)\pi$ contributions are also shown separately in Figs. 5(b)–5(d), respectively, and main contributions from the diagrams in Fig. 6 are also shown. The direct decays of Fig. 6(a) and single-rescattering mechanisms of Fig. 6(b) are obtained by perturbatively expanding the dressed η^* decay vertex of Fig. 1(c) in terms of V in Eq. (14), and taking the first two terms. The final $K^* \bar{K}$ contribution is mostly from the direct decay, while the final $\kappa \bar{K}$ and $a_0(980)\pi$ contributions are dominantly from the single-rescattering mechanism and therefore a coupled-channel effect. The $K^* \bar{K} K$ triangle loop causes a TS in the final $a_0(980)\pi$ contribution at $E \sim 1.4$ GeV. However, we do not find a large contribution from the TS. The TS-induced enhancement may have been suppressed since the $K^* \bar{K}$ pair is relatively p -wave.

Figure 7 illustrates the mechanism that creates the sharp $a_0(980)$ -like enhancement near the $K_S K_S$ threshold. Clearly, the final $K^* \bar{K}$ contribution alone creates the structure mostly, and the other mechanisms moderately change it. The final $a_0(980)\pi$ contribution is minor. As the Dalitz plots in Fig. 2 show, K^* and \bar{K}^* constructively interfere to generate a peak near the $K_S K_S$ threshold for $E = 1.45$ – 1.5 GeV. The $a_0(980)$ -like peaks seen at $E = 1.3$ – 1.45 GeV are also caused by the same mechanism.

The BESIII model obtained from their amplitude analysis describes the data rather differently from ours (see Fig. 3 of Ref. [29]): (i) the $a_0(980)\pi$ contribution is the largest overall, (ii) the $K^* \bar{K}$ contribution is comparable to

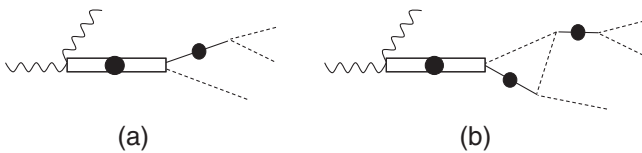


FIG. 6. Main η^* decay mechanisms included in Fig. 1(a): (a) direct decays and (b) single rescattering due to V of Eq. (14).

$a_0(980)\pi$ only around $E = 1.5$ GeV, and (iii) the $\kappa \bar{K}$ channel is not included. These differences come mainly from the fact that our model is fitted not only to the $K_S K_S \pi^0$ Dalitz plot pseudodata but also to the ratios of Eqs. (25) and (26); the BESIII model was fitted to the $J/\psi \rightarrow \gamma(K_S K_S \pi^0)$ data only. The ratio of Eq. (25), albeit a large uncertainty, is an important constraint on the final $a_0(980)\pi$ contribution to $\eta^* \rightarrow K \bar{K} \pi$, since the relative coupling of $a_0(980) \rightarrow K \bar{K}$ to $a_0(980) \rightarrow \pi \eta$ is experimentally determined in a certain range [15,46–49]. The final $a_0(980)\pi$ contribution to $K \bar{K} \pi$ needs to be small as in our model in order to satisfy the ratio of Eq. (25). Furthermore, the $\kappa \bar{K}$ channel in our model gives a substantial contribution through the channel coupling required by the unitarity.

Since the $a_0(980)\pi$ contribution is very different between our model and the BESIII model, one may wonder how much our result depends on a particular $a_0(980)$ model. As we discussed in Sec. III B, our default $a_0(980)$ model is based on Ref. [46] and $|g_{a_0(980) \rightarrow \kappa \bar{K}}/g_{a_0(980) \rightarrow \eta \pi}| \sim 1$.

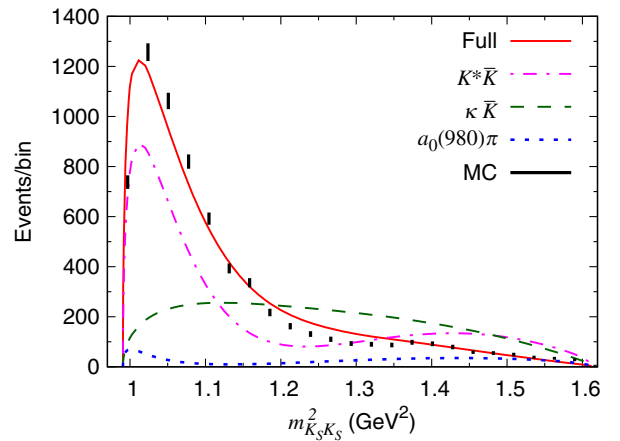


FIG. 7. Different final R_c contributions to the $K_S K_S$ invariant mass distribution at $E = 1405$ MeV.

The Particle Data Group (PDG) [15] considered two other analyses of Refs. [47,48] in averaging $\mathcal{B}(a_0(980) \rightarrow \eta\pi)/\mathcal{B}(a_0(980) \rightarrow K\bar{K})$. This ratio of the branchings can be translated into $|g_{a_0(980) \rightarrow K\bar{K}}/g_{a_0(980) \rightarrow \eta\pi}| \sim 0.77$ [47] and $|g_{a_0(980) \rightarrow K\bar{K}}/g_{a_0(980) \rightarrow \eta\pi}| \sim 0.85$ [48]. Thus, if we use an $a_0(980)$ model based on Refs. [47,48] in our present analysis, the corresponding $a_0(980)\pi$ contribution would be even smaller. There was also an analysis of $\gamma\gamma \rightarrow K\bar{K}, \eta\pi$ giving $|g_{a_0(980) \rightarrow K\bar{K}}/g_{a_0(980) \rightarrow \eta\pi}| \sim 2$ [49]. However, this analysis did not include $a_0(980) \rightarrow K\bar{K}$ data. Even if we use an $a_0(980)$ model based on this, our default result would not qualitatively change since the $a_0(980)\pi$ contribution could be at most ~ 4 times larger than our default result.

D. Fit with one bare η^* state

It is important to examine if the BESIII data can also be fitted with a single bare η^* model, since the $\eta(1405/1475)$ was claimed to be a single state in the literature. We try to fit only the $m_{K_S K_S \pi^0}(=E)$ distribution, but a reasonable fit is not achievable. The result is shown in Fig. 8 along with the final Rc contributions. The final $\kappa\bar{K}$ and $a_0\pi$ contributions have lineshapes expected from the η^* pole position, $1416 - 61i$ MeV. The TS caused by the $K^*\bar{K}K$ loop does not noticeably shift the lineshape of the final $a_0(980)\pi$ contribution. The peak of the lineshape of the final $K^*\bar{K}$ contribution is 30–40 MeV higher than the peak positions of the final $\kappa\bar{K}$ and $a_0(980)\pi$ contributions, since its threshold opens at $E \sim 1.4$ GeV and the $K^*\bar{K}$ pair is relatively p -wave. Still, the peak shift is not large enough to explain the significantly broader peak of the pseudodata.

Another possible single-state solution for $\eta(1405/1475)$ describes the BESIII data by including an interference with $\eta(1295)$. To examine this possibility, we include two bare η^* states, and restrict one of the bare masses below 1.4 GeV, and the other around 1.6 GeV. We are not able to obtain a reasonable fit to the pseudodata with this model. We thus

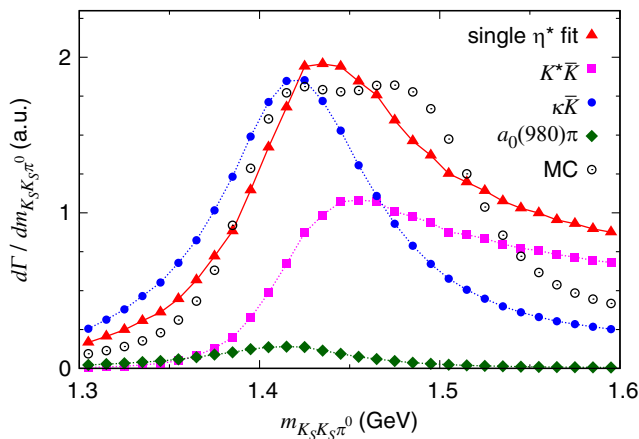


FIG. 8. Single bare η^* fit (red triangles) to the pseudodata (MC). Various final Rc contributions are also shown.

conclude that two bare η^* for $\eta(1405/1475)$ are necessary to reasonably fit the $K_S K_S \pi^0$ pseudodata generated from the BESIII 0^{-+} amplitude.

E. Pole positions for $\eta(1405)$ and $\eta(1475)$

The properties of a resonance are characterized by its pole position and residue of the (scattering or decay) amplitude. In the present unitary coupled-channel framework, a pole position corresponds to a complex energy E that satisfies $\det[\bar{G}^{-1}(E)] = 0$, where $\bar{G}^{-1}(E)$ has been defined in Eq. (15) and is analytically continued to the complex E plane. The analytic continuation involves deformations of the integral paths in Eqs. (9), (11), (13), and (16). Otherwise, singularities on the complex momentum planes cross the real momentum paths as E goes to complex values, invalidating the analytic continuation. The driving term $Z_{(c'R')\rho,(cR)_l}^{\bar{c},JPC}$ in Eq. (14) and $\tau_{R,R'}$ in Eqs. (11), (13), and (16) cause such singularities. To avoid these singularities, a possible deformed path to be used in Eqs. (11), (13), and (16) can be found in Fig. 7 of Ref. [42]. The energy denominator in Eq. (9) also causes a singularity and, for a complex E , we need to avoid it by choosing a deformed path as found in Fig. 3 of Ref. [42]. Our analytic continuation procedure is very similar to those discussed in detail in Ref. [42], and we do not go into it further.

We search for poles in the region of $\text{Re}[E] = 1300\text{--}1600$ MeV and $\text{Im}[-E] = 0\text{--}200$ MeV on the relevant Riemann sheets (RSs) close to the physical energy. We find three poles as listed in Table I. The poles are labeled by $\alpha = 1, 2$ [$\alpha = 3$] corresponding to $\eta(1405)$ [$\eta(1475)$]. The $\eta(1405/1475)$ poles are close to the branch points associated with the $K^*(892)\bar{K}$ and $a_2(1320)\pi$ thresholds at $\sim 1396 - 30i$ MeV and $\sim 1460 - 56i$ MeV, respectively. Thus, we specify the pole's RS of these channels in Table I; the relevant RS of the other channels should be clear.⁵ The locations of the poles and branch points are also shown in Fig. 9.

The BESIII analysis result (Breit-Wigner parameters) is also shown for comparison. A noticeable difference is that our model describes $\eta(1405)$ with two poles ($\alpha = 1, 2$). The two-pole structure does not mean two physical states but is simply due to the fact that a pole coupled to a channel is split into two poles on different RSs of this channel. The mass and width values are fairly similar between our results and the BESIII results. However, the use of the Breit-Wigner amplitude could cause an artifact due to the issues discussed in the introduction and below, which might explain the difference between the two analysis results. In Ref. [30], a unitary coupled-channel model and an isobar (Breit-Wigner) model were fitted to the same pseudodata. Resonance poles from the two

⁵For the definition of a (un)physical sheet, see the review section 50 “Resonances” in Ref. [15].

TABLE I. Locations of poles (E_{η^*}); each pole is labeled by α . The mass, width, and E_{η^*} are related by $M = \text{Re}[E_{\eta^*}]$ and $\Gamma = -2\text{Im}[E_{\eta^*}]$. Each pole is located on the RS specified by $(s_{K^*\bar{K}}, s_{a_2(1320)\pi})$; $s_x = p(u)$ indicates the physical (unphysical) sheet of a channel x . Breit-Wigner parameters from the BESIII analysis are also shown. Errors are statistical only. Table taken from Ref. [31].

	M (MeV)	Γ (MeV)	RS
$\alpha = 1$	1401.6 ± 0.6	65.8 ± 1.0	(up)
$\alpha = 2$	1401.6 ± 0.6	66.3 ± 0.9	(pp)
$\alpha = 3$	1495.0 ± 1.5	86.4 ± 1.8	(up)
BESIII [29]	1391.7 ± 0.7	60.8 ± 1.2	
	1507.6 ± 1.6	115.8 ± 2.4	

models can be significantly different, particularly when two resonances are overlapping. Also, if the pole is located near a threshold, the lineshape (E dependence) caused by the pole can be distorted by the branch cut. In the present case, $\eta(1405)$ and $\eta(1475)$ are fairly overlapping and $\eta(1405)$ is located near the $K^*\bar{K}$ threshold. Our three-body unitary coupled-channel analysis fully considers these issues and is a more appropriate pole-extraction method.

We examine the resonance pole contributions to the E distribution. For this purpose, we expand the dressed η^* propagator of Eq. (15) around the resonance pole at M_{R_α} as [50]

$$[\tilde{G}(E)]_{ij} \sim \frac{\chi_{\alpha,i}\chi_{\alpha,j}}{E - M_{R_\alpha}}, \quad (28)$$

with

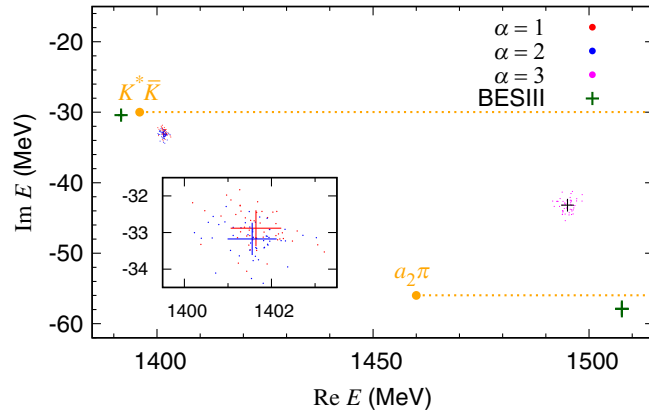


FIG. 9. Locations of $\eta(1405)$ and $\eta(1475)$ poles (labeled by α) from 50 bootstrap fits. Averaged locations of poles and their standard deviations are indicated by the crosses. The $K^*(892)\bar{K}$ and $a_2(1320)\pi$ branch points and cuts are shown by the orange circles and dotted lines, respectively. The BESIII result [29] (Breit-Wigner parameters) is shown by the green crosses. The inset shows the $\alpha = 1, 2$ region. Figure taken from Ref. [31].

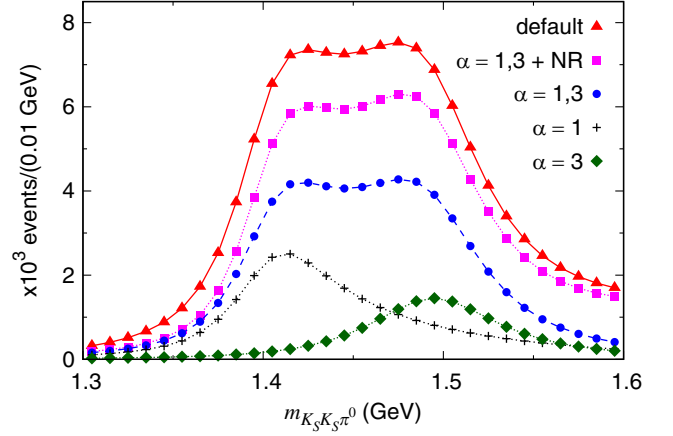


FIG. 10. Pole contributions from $\eta(1405)$ ($\alpha = 1$) and $\eta(1475)$ ($\alpha = 3$) and their coherent sum ($\alpha = 1, 3$) to the $m_{K_S K_S \pi^0}$ distribution. The poles labeled by α are listed in Table I. The NR contribution is from Eq. (27).

$$\chi_{\alpha,1} = \sqrt{\frac{M_{R_\alpha} - m_{\eta_2^*} - [\Sigma_{\eta^*}(M_{R_\alpha})]_{22}}{\Delta'(M_{R_\alpha})}}, \quad (29)$$

$$\chi_{\alpha,2} = \frac{[\Sigma_{\eta^*}(M_{R_\alpha})]_{12}}{M_{R_\alpha} - m_{\eta_2^*} - [\Sigma_{\eta^*}(M_{R_\alpha})]_{22}} \chi_{\alpha,1}, \quad (30)$$

$\Delta(E) \equiv \det[\tilde{G}^{-1}(E)]$, and $\Delta'(M_{R_\alpha}) = d\Delta(E)/dE|_{E=M_{R_\alpha}}$. Then, we replace $\tilde{G}_{ij}(E)$ in the full amplitude of Eq. (2) with the above expanded form and calculate the $m_{K_S K_S \pi^0}$ distribution. In Fig. 10, we show each of the pole contributions and their coherent sum, in comparison with the full calculation. The $\alpha = 2$ pole contribution is not included in the figure since the $K^*\bar{K}$ branch cut mostly screens this pole contribution to the amplitude on the physical real E axis. The contributions from the $\alpha = 1$ and 3 poles are dominant, and the lineshape of the full calculation is mostly formed by the pole contributions. The nonresonant term in Eq. (27) enhances the spectrum overall through the interference. Still, the branch cuts and nonpole contribution are missing in the pole approximation of Eq. (28), and their effects should explain the difference between the red triangles and the magenta squares in the figure.

The resonance amplitude of Eq. (28) suggests that one of the pole contributions can be eliminated from our full model by adjusting the coupling $g_{J/\psi\eta_1^*\gamma}$ in the initial vertex of Eq. (4). Specifically, we can eliminate the contribution of the pole α by setting

$$g_{J/\psi\eta_2^*\gamma} = -(\chi_{\alpha,1}/\chi_{\alpha,2})g_{J/\psi\eta_1^*\gamma}, \quad (31)$$

as demonstrated in Fig. 11(a). The figure shows a full calculation without the pole approximation of Eq. (28). Eliminating the initial radiative transition of $J/\psi \rightarrow [\alpha = 1]$, we obtain the magenta squares ($g_{J/\psi[\alpha=1]\gamma} = 0$) showing a

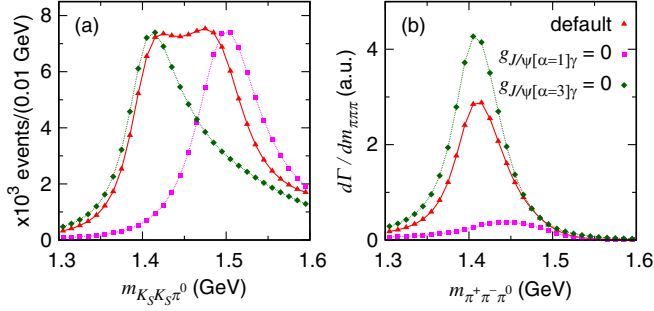


FIG. 11. (a) $m_{K_S K_S \pi^0}$ and (b) $m_{\pi^+ \pi^- \pi^0}$ distributions from $J/\psi \rightarrow \gamma(0^{-+}) \rightarrow \gamma(K_S K_S \pi^0)$ and $\gamma(\pi^+ \pi^- \pi^0)$, respectively, obtained with various choices of $g_{J/\psi \eta^* \gamma}$ in Eq. (4). The red triangles in panels (a) and (b) are the same as those in Figs. 5(a) and 16(a), respectively. With the coupling to the $\alpha = 1$ ($\alpha = 3$) pole eliminated, the magenta squares (green diamonds) are obtained. All of the calculations in panel (a) use normalized $g_{J/\psi \eta^* \gamma}$ values to have the same peak height. The same legends in panels (a) and (b) share the same $g_{J/\psi \eta^* \gamma}$.

single peak from the $\alpha = 3$ pole. Similarly, a calculation with $g_{J/\psi[\alpha=3]\gamma} = 0$ gives the green diamonds that have a single peak from the $\alpha = 1$ pole.

Among various processes that include $\eta(1405/1475)$ -decay into $K\bar{K}\pi$ final states, some of them show a single peak from either of $\eta(1405)$ or $\eta(1475)$, and others have a broad peak from a coherent sum of them. Figure 11(a) indicates that our coupled-channel model can describe both cases by appropriately adjusting the couplings of initial vertices.

In the presented analysis, two bare states are required to reasonably fit the data set. The lighter bare mass is determined to be ~ 1.6 GeV, while the heavier one is ~ 2.3 GeV, as listed in Table IX of Appendix B. The heavier bare mass is not tightly constrained by the fit, and those in the range of 2–2.4 GeV can give comparable

fits. Within our coupled-channel model, the bare states are mixed and dressed by meson-meson continuum states, forming the resonance states. In concept, the bare states are similar to states from a quark model or LQCD without two-hadron operators. The lighter bare state seems compatible with the excited $s\bar{s}$ [15,16,23]. The heavier bare state could be either a second radial excitation of $\eta^{(\prime)}$, a hybrid [23], a glueball [18–22], or a mixture of these states.

IV. PREDICTIONS FOR

$$J/\psi \rightarrow \gamma(0^{-+}) \rightarrow \gamma(\pi\pi\eta), \gamma(\pi^+ \pi^- \gamma), \gamma(\pi\pi\pi)$$

In this section, we present E dependences of various final states from the radiative J/ψ decays via $\eta(1405/1475)$, using the three-body unitary coupled-channel model developed in the previous section. The model has been fitted to the $K_S K_S \pi^0$ Dalitz plot pseudodata (Fig. 2) and the ratios of Eqs. (25) and (26).

A. $\pi^+ \pi^- \eta$ and $\pi^0 \pi^0 \eta$ final states

We show in Fig. 12(a) the $m_{\pi\pi\eta}(=E)$ distributions for the $\pi^+ \pi^- \eta$ final state; the $\pi^0 \pi^0 \eta$ distribution is smaller by a factor of 1/2. The lineshape is qualitatively consistent with the MARK III analysis [3]. The final $a_0(980)\pi$ and $f_0\eta$ states have comparable contributions. On the other hand, the $K\bar{K}\pi$ final states are mainly from the final $K^* \bar{K}$ and $\kappa \bar{K}$ contributions, as seen in Fig. 5(a). Since different Rc final states couple with $\eta(1405)$ and $\eta(1475)$ differently, the $K\bar{K}\pi$ and $\pi\pi\eta$ final states have different E dependences. The $\pi\pi\eta$ final states give a single peak at $m_{\pi\pi\eta} \sim 1.4$ GeV, while the $K\bar{K}\pi$ distribution has a flat peak. The process-dependent lineshape of the $\eta(1405/1475)$ decays can thus be understood.

In Figs. 12(b) and 12(c), we decompose the final $a_0(980)\pi$ and $f_0\eta$ contributions into direct decays [Fig. 6(a)] and single-rescattering mechanisms [Fig. 6(b)]. The final $a_0(980)\pi$ state is mostly from the single-rescattering

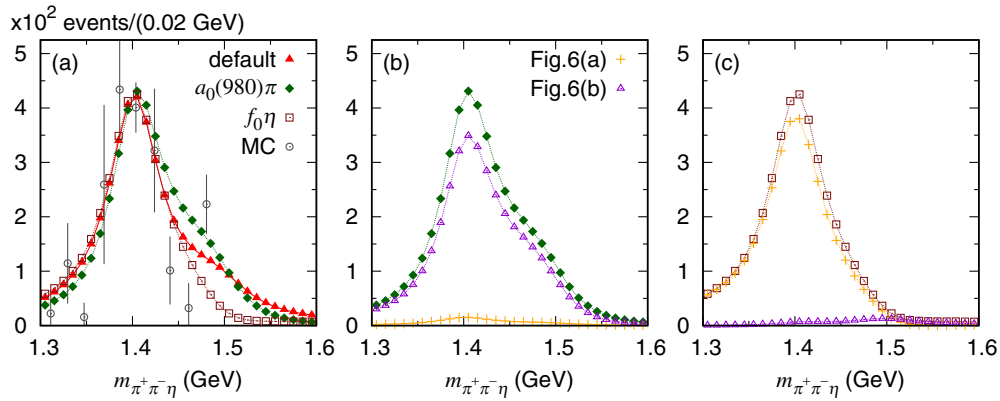


FIG. 12. $m_{\pi\pi\eta}(=E)$ distribution for $J/\psi \rightarrow \gamma(0^{-+}) \rightarrow \gamma(\pi^+ \pi^- \eta)$. (a) The default model prediction and final $a_0(980)\pi$ and $f_0\eta$ contributions are shown. The MC output is from Ref. [3]. (b) [(c)] The final $a_0(980)\pi$ [$f_0\eta$] contribution. Main contributions from the diagrams of Figs. 6(a) and 6(b) are also shown. Figure 12(a) is taken from Ref. [31].

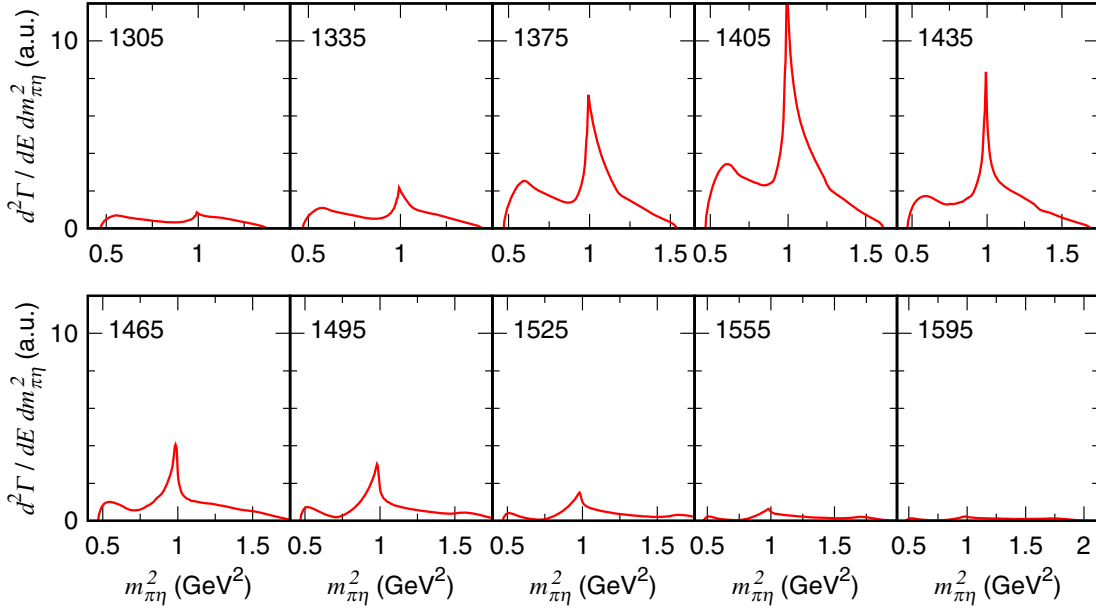


FIG. 13. $m_{\pi\eta}^2$ distribution for $J/\psi \rightarrow \gamma(0^{++}) \rightarrow \gamma(\pi^+\pi^-\eta)$ from the default model. The E value is indicated in each panel.

mechanisms and the direct decays are minor. On the other hand, a completely opposite trend applies to the final $f_0\eta$ state. In more detail, the $K^*K\bar{K}$, $\kappa K\bar{K}$, and $f_0\pi\eta$ triangle mechanisms contribute to the final $a_0(980)\pi$ state. We find that the three loops give comparable contributions, even though only the $K^*K\bar{K}$ loop causes a TS. This is perhaps because the $K^*\bar{K}$ pair is relatively p -wave, suppressing the TS.

We also present in Fig. 13 a prediction for the $m_{\pi\eta}^2$ distribution from the default model. Clear $a_0(980)$ peaks are predicted, which is qualitatively consistent with the data [4]. This prediction should be confronted with future data from BESIII.

As already discussed, the final $a_0(980)\pi$ contribution to the $K\bar{K}\pi$ and $\pi\pi\eta$ final states are related by the relative coupling of $a_0(980) \rightarrow K\bar{K}$ to $a_0(980) \rightarrow \pi\eta$ determined experimentally [15,46–49]. As we have seen in Fig. 5(a), the final $a_0(980)\pi$ contribution to $K\bar{K}\pi$ is very small to satisfy the ratio of Eq. (25). If the final $a_0(980)\pi$ contribution to $K\bar{K}\pi$ were as large as that of the BESIII amplitude model, then Eq. (25) would require that the final $a_0(980)\pi \rightarrow \pi\pi\eta$ amplitude has to be drastically canceled by destructively interfering with the final $f_0\eta \rightarrow \pi\pi\eta$ amplitude. Such a large cancellation seems unlikely since there is no symmetry behind. Also, the large cancellation makes the $a_0(980)$ peak in the $m_{\pi\eta}$ distribution rather unclear, but the data [4] shows a clear $a_0(980)$ peak. As shown in Fig. 13, our default model creates a clear $a_0(980)$ peak.

B. $\pi^+\pi^-\gamma$ final state

The branching to $J/\psi \rightarrow \gamma(0^{++}) \rightarrow \gamma(\pi^+\pi^-\gamma)$ in the default model is constrained by the ratio of Eq. (26).

Then, the model predicts the E distribution as shown in Fig. 14. The lineshape has a single peak at $E \sim 1.4$ GeV, being consistent with the previous data [8,9]. The process is mostly from a sequence of $\eta_i^* \rightarrow \rho^0\rho^0$ followed by $\rho^0 \rightarrow \gamma$ and $\rho^0 \rightarrow \pi^+\pi^-$. Thus, $\eta(1405)$ couples to $\rho\rho$ much more strongly than $\eta(1475)$ does, implying different natures of the two η^* resonances. Also, as mentioned in Sec. III B, only the heavier bare η^* couples with $\rho\rho$. This implies that $\eta(1405)$ includes a larger content of the heavier bare η^* than $\eta(1475)$ does.

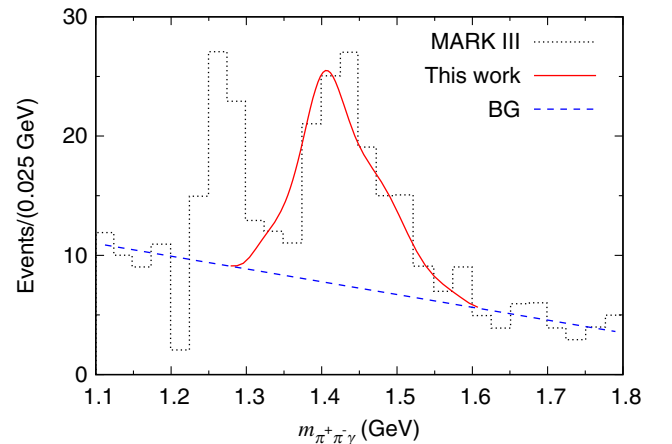


FIG. 14. $m_{\pi^+\pi^-\gamma}(=E)$ distribution of $J/\psi \rightarrow \gamma(0^{++}) \rightarrow \gamma(\pi^+\pi^-\gamma)$ where the $\pi^+\pi^-$ pair is from ρ^0 decay. The default model predicts the lineshape of the red curve which has been smeared with the experimental bin width, scaled by a factor, and augmented by a linear background (BG) to fit the data [9].

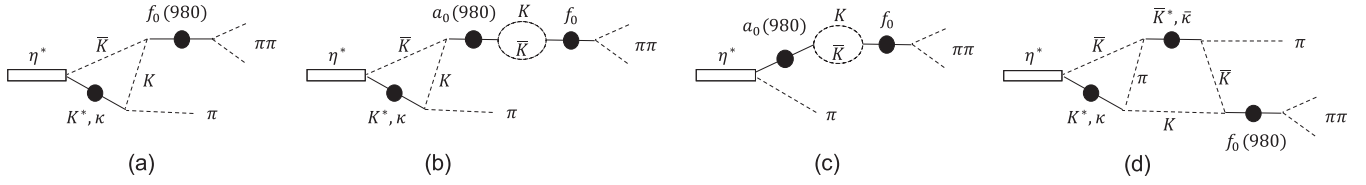


FIG. 15. Main mechanisms for isospin-violating $\eta^* \rightarrow \pi\pi\pi$ decay included in Fig. 1(c): (a) isospin-violating $K^*(\kappa)\bar{K}K$ triangle loop, (b) isospin-conserving $K^*(\kappa)\bar{K}K$ triangle loop followed by a_0 - f_0 mixing, (c) direct decay to $a_0(980)\pi$ followed by a_0 - f_0 mixing, and (d) isospin-conserving $K^*(\kappa)\bar{K}\pi$ triangle loop followed by isospin-violating $\pi\bar{K}^*(\bar{\kappa})K\bar{K}$ box loop.

C. $\pi^+\pi^-\pi^0$ and $\pi^0\pi^0\pi^0$ final states

Our default model makes predictions for the isospin-violating $J/\psi \rightarrow \gamma(0^{+-}) \rightarrow \gamma(\pi\pi\pi)$; the model has not been constrained by any data of the $\pi\pi\pi$ final states. These isospin-violating processes are mainly from the mechanisms of Fig. 15 that are not completely canceled due to the small difference between the charged and neutral K masses. In particular, the isospin-violating mechanisms in Figs. 15(b) and 15(c) are called the a_0 - f_0 mixing. The $m_{\pi\pi\pi}$ distributions are shown in Fig. 16(a). The $\pi^+\pi^-\pi^0$ distribution is almost twice as large as the $\pi^0\pi^0\pi^0$ distribution. The $m_{\pi\pi\pi}$ distributions have a single peak at ~ 1.4 GeV.

Contributions from the diagrams of Figs. 15(a)–15(d) are separately shown in Fig. 16(b). The $K^*(\kappa)\bar{K}K$ triangle loop diagram of Fig. 15(a) generates a clear peak. As has been discussed in the literature, this $K^*\bar{K}K$ triangle loop is significantly enhanced by a TS occurring at $E \sim 1.40$ GeV. The $\kappa\bar{K}K$ triangle loop without a TS gives a smaller contribution. The TS enhancement is larger around the higher end of the TS energy range since the p -wave $K^*\bar{K}$ pair suppresses the TS enhancement around the lower end. This explains the peak position in Fig. 16.

The a_0 - f_0 mixing contribution is very small. This is because $\eta(1405/1475) \rightarrow a_0(980)\pi$ is very little as seen in Fig. 5(a). This small branching is required by the experimental ratio of Eq. (25). The two-loop mechanisms of Fig. 15(d) are sizable; the second loop involves a TS. A part

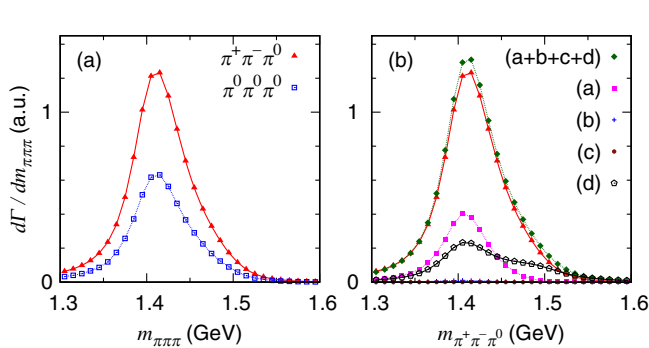


FIG. 16. $m_{\pi\pi\pi}(=E)$ distributions for $J/\psi \rightarrow \gamma(0^{+-}) \rightarrow \gamma(\pi\pi\pi)$ predicted by the default model. (a) line shapes and relative magnitudes of the $\pi^+\pi^-\pi^0$ and $\pi^0\pi^0\pi^0$ final states. (b) Contributions to the $\pi^+\pi^-\pi^0$ final state from the diagrams in Figs. 15(a)–15(d).

of the two-loop contribution is from mechanisms where the two loops are mediated by v^{HLS} in Eq. (14). The coherent sum of the mechanisms in Fig. 15 (green diamonds in Fig. 16) mostly explain the full calculation (red triangles).

We confront our predictions for the $\pi^+\pi^-\pi^0$ and $\pi^0\pi^0\pi^0$ lineshapes with the BESIII data [24] in Figs. 17(a) and 17(b), respectively. Our model correctly predicts the peak position. This remarkable agreement suggests that the peak position is determined by a kinematical effect (TS) that does not depend on dynamical details. However, the peak width from our calculation seems somewhat broader than the data; we will come back to this point later.

In Fig. 18, we also compare the $m_{\pi^+\pi^-}$ distribution from our full calculation with the BESIII data [24]. Again, the agreement is reasonable, showing the sound predictive power of the coupled-channel model that appropriately consider the relevant kinematical effect for the isospin violation. The $f_0(980)$ -like peak width (~ 10 MeV) is much narrower than the world average (~ 50 MeV) [15]. This occurs because the $(K^*)K^+K^-$ and $(K^*)K^0\bar{K}^0$ loops in Fig. 15 almost exactly cancel with each other due to the isospin symmetry, except in a small window (~ 8 MeV) of $2m_{K^\pm} \pm m_{\pi\pi} < 2m_{K^0}$ where the two loops are rather different and the cancellation is incomplete. Furthermore, the TS enhances the $f_0(980)$ -like peak. Therefore, the $f_0(980)$ pole plays a minor role in developing the peak in Fig. 18.

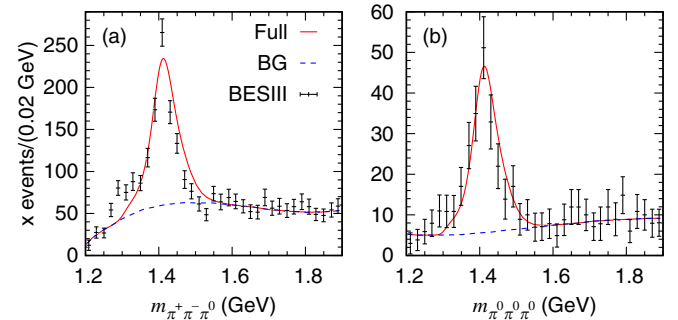


FIG. 17. $m_{\pi\pi\pi}(=E)$ distributions for $J/\psi \rightarrow \gamma(0^{+-}) \rightarrow \gamma(\pi\pi\pi)$ in comparison with the BESIII data [24] for (a) $\pi^+\pi^-\pi^0$ and (b) $\pi^0\pi^0\pi^0$ final states. The full calculations are smeared with the bin width, scaled to fit the data, and augmented by the background polynomials (BG) from Ref. [24]. Figure 17(a) is taken from Ref. [31].

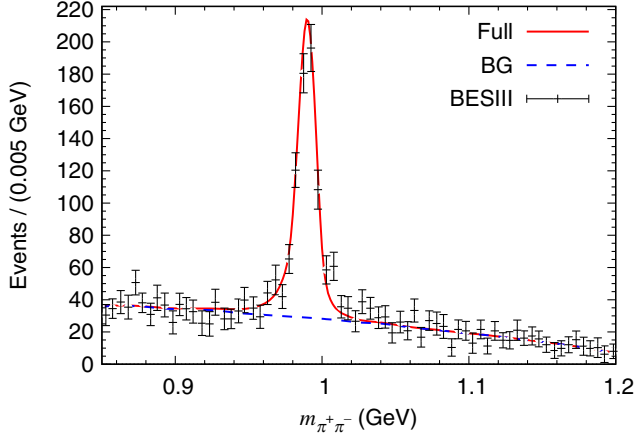


FIG. 18. $m_{\pi^+\pi^-}$ distribution of $J/\psi \rightarrow \gamma(0^{++}) \rightarrow \gamma(\pi^+\pi^-\pi^0)$. The BESIII data and the background polynomial (BG) are from Ref. [24]. Our full calculation has been smeared with the bin width, scaled to fit the data, and augmented by the background. Figure taken from Ref. [31].

How do $\eta(1405)$ and $\eta(1475)$ resonances work in $J/\psi \rightarrow \gamma(\pi\pi\pi)$? We address this question by using the models shown in Fig. 11(a). In the figure, the models labeled by $g_{J/\psi[\alpha=1]\gamma} = 0$ and $g_{J/\psi[\alpha=3]\gamma} = 0$ do not have $J/\psi \rightarrow \gamma\eta(1405)$ and $J/\psi \rightarrow \gamma\eta(1475)$ couplings, respectively, and they are normalized to have the same peak height in the $m_{K_S K_S \pi^0}$ distribution. Then, we use them to calculate $J/\psi \rightarrow \gamma(\pi^+\pi^-\pi^0)$ as shown in Fig. 11(b). For the model of $g_{J/\psi[\alpha=3]\gamma} = 0$, the peak positions are almost the same for $K\bar{K}\pi$ and $\pi\pi\pi$ final states. This is because $\eta(1405) \rightarrow \pi\pi\pi$ is dominant and the $\eta(1405)$ mass and the TS region overlap well. However, the peak width is narrower for $\pi\pi\pi$ because the TS region is narrower than the $\eta(1405)$ width. On the other hand, the model of $g_{J/\psi[\alpha=1]\gamma} = 0$ gives a significantly suppressed $m_{\pi\pi\pi}$ distribution in comparison with the model of $g_{J/\psi[\alpha=3]\gamma} = 0$. This is because the $\eta(1475)$ mass is outside of the TS region and $\eta(1475) \rightarrow \pi\pi\pi$ is not enhanced. In this way, we understand the origins of the different $K\bar{K}\pi$ and $\pi\pi\pi$ lineshapes in Fig. 11.

Finally, we compare ratios of $K\bar{K}\pi$ and $\pi\pi\pi$ branching fractions from our model with the experimental counterparts. Using the $K\bar{K}\pi$ and $\pi\pi\pi$ branching ratios in Refs. [15,24], we have the experimental ratios

$$\begin{aligned} R_3^{\text{exp}} &= \frac{\Gamma[J/\psi \rightarrow \gamma\eta(1405/1475) \rightarrow \gamma(\pi^+\pi^-\pi^0)]}{\Gamma[J/\psi \rightarrow \gamma\eta(1405/1475) \rightarrow \gamma(K\bar{K}\pi)]} \\ &= \frac{(1.50 \pm 0.11 \pm 0.11) \times 10^{-5}}{(2.8 \pm 0.6) \times 10^{-3}} \\ &= 0.004 - 0.007, \end{aligned} \quad (32)$$

and

$$\begin{aligned} R_4^{\text{exp}} &= \frac{\Gamma[J/\psi \rightarrow \gamma\eta(1405/1475) \rightarrow \gamma(\pi^0\pi^0\pi^0)]}{\Gamma[J/\psi \rightarrow \gamma\eta(1405/1475) \rightarrow \gamma(K\bar{K}\pi)]} \\ &= \frac{(7.10 \pm 0.82 \pm 0.72) \times 10^{-6}}{(2.8 \pm 0.6) \times 10^{-3}} \\ &= 0.002 - 0.003. \end{aligned} \quad (33)$$

Our coupled-channel model predicts

$$R_3^{\text{th}} = 0.0020 - 0.0021, \quad R_4^{\text{th}} = 0.0010 - 0.0011, \quad (34)$$

which is significantly smaller than the data. A possible reason for the deficit is that we do not consider a contribution from the $J^{PC} = 1^{++}$ partial wave that includes $f_1(1285)$ and $f_1(1420)$. The BESIII analysis [29] found that 20–30% of $J/\psi \rightarrow \gamma(K_S K_S \pi^0)$ is from the 1^{++} contribution in which $f_1(1420) \rightarrow K^* \bar{K}$ is a dominant mechanism. Considering the consistency with $J/\psi \rightarrow \gamma(K\bar{K}\pi)$, $J/\psi \rightarrow \gamma(\pi\pi\pi)$ should come not only from the mechanisms of Fig. 15 but also from similar mechanisms that originate from f_1 decays. In particular, the triangle diagram from the $f_1(1420)$ decay similar to Fig. 15(a) would be significantly enhanced by the TS, since the $f_1(1420)$ mass and width have a good overlap with the TS region. Furthermore, $f_1(1420)$ creates an s -wave $K^* \bar{K}$ pair while $\eta(1405)$ creates a p -wave pair. Thus, the triangle mechanism from $f_1(1420)$ is more enhanced by the TS than that from $\eta(1405)$. This 1^{++} contribution might explain the difference between our prediction of Eq. (34) and the experimental ratios of Eqs. (32) and (33). We also note that the BESIII [24] did not separate out a possible $f_1(1420)$ contribution from $\Gamma[J/\psi \rightarrow \gamma\eta(1405/1475) \rightarrow \gamma(\pi\pi\pi)]$ in Eqs. (32) and (33). The stronger TS enhancement would create a sharper peak in the $m_{\pi\pi\pi}$ lineshape. In Fig. 17, our 0^{++} model shows a peak that is somewhat broader than the data. By adding a sharper 1^{++} peak, the data might be better fitted.

V. SUMMARY AND FUTURE PROSPECTS

Whether $\eta(1405/1475)$ is one or two states has been a controversial issue. The recent BESIII amplitude analysis of $J/\psi \rightarrow \gamma K_S K_S \pi^0$ made important progress by claiming two states with a high confidence level. This analysis was based on $\sim 10^{10}$ J/ψ decay samples which is significantly more precise than earlier $\eta(1405/1475)$ -related data. However, the BESIII analysis used a simple Breit-Wigner amplitude for $\eta(1405/1475)$. For a more reliable determination of the $\eta(1405/1475)$ poles and their decay dynamics, a three-body unitary coupled-channel analysis is desirable.

Thus, we developed a model for radiative J/ψ decays to three pseudoscalar-meson final states of any partial wave (J^{PC}). Also, a slight extension was made to include the $\gamma\rho(\rho \rightarrow \pi^+\pi^-)$ final state. The main components of the model are two-body πK , $\pi\pi$, $K\bar{K}$, and $\pi\eta$ scattering models that generate $K_0^*(700)(=\kappa)$, $K^*(892)$, $f_0(500)(=\sigma)$,

$f_0(980)$, $a_0(980)$, and $a_2(1320)$ resonance poles in the scattering amplitudes. The two-body scattering models as well as bare resonance states were implemented into the three-body coupled-channel scattering equation (Faddeev equation). By solving the equation, we obtained the three-body unitary amplitudes with which we described the final-state interactions in the radiative J/ψ decays.

Using BESIII's $J^{PC} = 0^{-+}$ amplitude for $J/\psi \rightarrow \gamma K_S K_S \pi^0$, we generated $K_S K_S \pi^0$ Dalitz plot pseudodata for 30 energy bins in $1.3 \text{ GeV} \leq m_{K_S K_S \pi^0} \leq 1.6 \text{ GeV}$. Then, the pseudodata were fitted with the coupled-channel model. The experimental branching ratios of $\eta(1405/1475) \rightarrow \eta\pi\pi$ and $\eta(1405/1475) \rightarrow \gamma\rho$ relative to that of $\eta(1405/1475) \rightarrow K\bar{K}\pi$ were simultaneously fitted. We obtained a reasonable fit with two bare η^* states, while we did not find a reasonable solution with one bare η^* state. A noteworthy difference from the BESIII amplitude model is that the $a_0(980)\pi$ contribution is dominant (very small) in the BESIII (our) model. The small $a_0(980)\pi$ contribution is required by the empirical branching ratio of $\eta(1405/1475) \rightarrow \eta\pi\pi$ that was not considered in the BESIII analysis.

Our 0^{-+} amplitude was analytically continued to reach three poles in the $\eta(1405/1475)$ region. Two poles corresponding to $\eta(1405)$ were found near the $K^*\bar{K}$ threshold, and are located on different RRs of the $K^*\bar{K}$ channel. Another pole is $\eta(1475)$. We made 50 bootstrap fits, and estimated statistical uncertainties of the pole positions (Table I). This is the first pole determination of $\eta(1405/1475)$ and, furthermore, the first-ever pole determination from analyzing experimental Dalitz plot distributions with a manifestly three-body unitary coupled-channel framework.

The obtained model was used to predict the $\eta\pi\pi$ and $\gamma\pi^+\pi^-$ lineshapes of $J/\psi \rightarrow \gamma(0^{-+}) \rightarrow \gamma(\eta\pi\pi)$ and $\gamma(\gamma\rho)$ processes. The predicted lineshapes are process-dependent and reasonably consistent with the existing data. We also applied the model to the isospin-violating $J/\psi \rightarrow \gamma(0^{-+}) \rightarrow \gamma(\pi\pi\pi)$. The importance of the TS from the $K^*\bar{K}K$ loop was clarified, while the $a_0(980)$ - $f_0(980)$ mixing gave a tiny contribution. Furthermore, the two-loop contribution was calculated for the first time, and this contribution was shown to significantly enhance the isospin violation. The predicted $\pi\pi\pi$ and $\pi^+\pi^-$ lineshapes agree well with the BESIII data. Although the predicted branching fraction underestimates the data, we may expect the 1^{++} partial wave including $f_1(1420)$ to fill the deficiency.

Here, we stress that all of the above conclusions are based on the Dalitz plot pseudodata including only the 0^{-+} contribution, and on the current branching ratios of $\eta(1405/1475) \rightarrow \eta\pi\pi$ and $\eta(1405/1475) \rightarrow \gamma\rho$ relative to that of $\eta(1405/1475) \rightarrow K\bar{K}\pi$. Since all of this experimental information was extracted with simpler Breit-Wigner models, our results might be biased. This situation encourages further studies.

In the next step, we will extend the present analysis by including more partial waves such as 1^{++} and 2^{++} , and directly analyze the BESIII data on $J/\psi \rightarrow \gamma K_S K_S \pi^0$. Then, we can perform the partial-wave decomposition with our unitary coupled-channel framework by ourselves. With the 0^{-+} amplitude obtained in this way, the two-pole solution of $\eta(1405/1475)$ needs to be reexamined. Also, we can consistently study the relevant resonances such as $\eta(1405/1475)$ and $f_1(1420)$ with the unitary coupled-channel framework.

Our model can be easily applied to other decay processes that could involve $\eta(1405/1475)$ by simply changing the initial vertex of Eq. (4) and keeping the rest the same. These processes include $\psi(2S) \rightarrow \omega(K\bar{K}\pi)$ [51], $\psi(2S) \rightarrow \phi(\eta\pi\pi)$ [52], $J/\psi \rightarrow \omega(\eta\pi^+\pi^-)$ [53], $J/\psi \rightarrow \omega(K\bar{K}\pi)$, $\phi(K\bar{K}\pi)$, $\eta(K_S^0 K^\pm \pi^\mp)$ [54], and $\chi_{c0} \rightarrow \eta(\pi\pi\eta)$, $\eta(K\bar{K}\pi)$. It would be important to analyze these various processes to establish the nature of $\eta(1405/1475)$.

ACKNOWLEDGMENTS

We acknowledge Y. Cheng, M.-C. Du, S.-S. Fang, F.-K. Guo, Y.-P. Huang, H.-B. Li, B. Liu, X.-R. Lyu, W.-B. Qian, L. Qiu, X.-Y. Shen, J.-J. Xie, G.-F. Xu, Q. Zhao, and B.-S. Zou for useful discussions. This work is supported in part by the National Natural Science Foundation of China (NSFC) under contracts U2032103, 11625523, 12175239, 12221005, 12305087, and U2032111, and also by the National Key Research and Development Program of China under Contracts 2020YFA0406400, the Chinese Academy of Sciences under Grant No. YSBR-101 (J.-J. W.), and the Start-up Funds of Nanjing Normal University under Grant No. 184080H201B20 (Q. H.).

APPENDIX A: TWO-MESON SCATTERING MODELS

1. Formulas

We develop a unitary coupled-channel model for each of the $\pi\pi$, πK , and $\pi\eta$ partial-wave scatterings. Let us consider a $ab \rightarrow a'b'$ scattering with total energy E . A partial wave is specified by the total angular momentum L and total isospin I . The incoming and outgoing momenta are denoted by q and q' , respectively. Suppose that the scattering can be described with a contact interaction

$$v_{a'b',ab}^{LI}(q',q) = w_{a'b'}^{LI}(q') h_{a'b',ab}^{LI} w_{ab}^{LI}(q), \quad (\text{A1})$$

where $h_{a'b',ab}^{LI}$ is a coupling constant. We also introduce a vertex function $w_{ab}^{LI}(q)$ in the form of

$$w_{ab}^{LI}(q) = \frac{1}{\sqrt{\mathcal{B}_{ab}}} \frac{[1 + (q/b_{ab}^{LI})^2]^{-2-L/2}}{\sqrt{E_a(q)E_b(q)}} \left(\frac{q}{m_\pi}\right)^L, \quad (\text{A2})$$

where b_{ab}^{LI} is a cutoff and \mathcal{B}_{ab} is a factor associated with the Bose symmetry, with $\mathcal{B}_{ab} = 1/2$ for identical particles a and b and $\mathcal{B}_{ab} = 1$ otherwise. The partial-wave amplitude is then given by

$$t_{a'b',ab}^{LI}(q', q; E) = \sum_{a''b''} w_{a'b'}^{LI}(q') \tau_{a'b',a''b''}^{LI}(E) \times h_{a''b'',ab}^{LI} w_{ab}^{LI}(q), \quad (\text{A3})$$

with

$$[(\tau^{LI}(E))^{-1}]_{a'b',ab} = \delta_{a'b',ab} - \sigma_{a'b',ab}^{LI}(E), \quad (\text{A4})$$

$$\sigma_{a'b',ab}^{LI}(E) = \int dq q^2 \frac{\mathcal{B}_{ab} h_{a'b',ab}^{LI} [w_{ab}^{LI}(q)]^2}{E - E_a(q) - E_b(q) + i\epsilon}. \quad (\text{A5})$$

Next, we also include bare R excitation mechanisms in the interaction as

$$V_{a'b',ab}^{LI}(q', q; E) = \sum_R f_{a'b',R}^{LI}(q') \frac{1}{E - m_R} f_{R,ab}^{LI}(q) + v_{a'b',ab}^{LI}(q', q), \quad (\text{A6})$$

with m_R being the bare R mass. A bare $R \rightarrow ab$ vertex function is denoted by $f_{ab,R}^{LI}(q)$ and $f_{R,ab}^{LI}(q) = f_{ab,R}^{LI}(q)$; an explicit form is given in Eq. (7). With the interaction of Eq. (A6), the resulting scattering amplitude is given by

$$T_{a'b',ab}^{LI}(q', q; E) = \sum_{R',R} \bar{f}_{a'b',R'}^{LI}(q'; E) \tau_{R',R}^{LI}(0, E) \bar{f}_{R,ab}^{LI}(q; E) + t_{a'b',ab}^{LI}(q', q; E). \quad (\text{A7})$$

The second term is given in Eq. (A3). The dressed $R \rightarrow ab$ vertex, denoted by $\bar{f}_{ab,R}$, is given by

$$\bar{f}_{ab,R}^{LI}(q; E) = f_{ab,R}^{LI}(q) + \sum_{a'b'} \int dq' q'^2 \times \frac{\mathcal{B}_{a'b'} t_{ab,a'b'}^{LI}(q, q'; E) f_{a'b',R}^{LI}(q')}{E - E_{a'}(q') - E_{b'}(q') + i\epsilon}, \quad (\text{A8})$$

$$\bar{f}_{R,ab}^{LI}(q; E) = f_{R,ab}^{LI}(q) + \sum_{a'b'} \int dq' q'^2 \times \frac{\mathcal{B}_{a'b'} f_{R,a'b'}^{LI}(q') t_{a'b',ab}^{LI}(q', q; E)}{E - E_{a'}(q') - E_{b'}(q') + i\epsilon}. \quad (\text{A9})$$

The dressed Green function for R , $\tau_{R',R}^{LI}(p, E)$, in Eq. (A7) is given in Eqs. (8) and (9) with $f_{ab,R'}$ being replaced by $\bar{f}_{ab,R'}$.

The partial-wave amplitude $T_{a'b',ab}^{LI}$ in Eq. (A7) is related to the S -matrix by

$$s_{ab,ab}^{LI}(E) = \eta_{LI} e^{2i\delta_{LI}} = 1 - 2\pi i \rho_{ab} \mathcal{B}_{ab} T_{ab,ab}^{LI}(q_o, q_o; E), \quad (\text{A10})$$

where δ_{LI} and η_{LI} are the phase shift and inelasticity, respectively, q_o is the on-shell momentum ($E = E_a(q_o) + E_b(q_o)$), and $\rho_{ab} = q_o E_a(q_o) E_b(q_o) / E$ is the phase-space factor.

2. Fits to $\pi\pi$, πK , and $\pi\eta$ scattering data

In our unitary coupled-channel model for describing the radiative J/ψ decays in the $\eta(1405/1475)$ region, $\pi\pi - K\bar{K}$, πK , and $\pi\eta - K\bar{K}$ coupled-channel scattering amplitudes of $E \lesssim 1.2$ GeV are the major components. Our choices for the scattering models such as the number of R and contact interactions are specified in Table II. We determine the parameters in the two-meson scattering models such as $h_{a'b',ab}^{LI}$, b_{ab}^{LI} , m_R , $g_{ab,R}$, and $c_{ab,R}$ in Eqs. (A1), (A6), and (7) using experimental information. For the $\pi\pi - K\bar{K}$ and πK s - and p -wave scattering amplitudes, we fit empirical scattering amplitudes by adjusting the model parameters and obtain reasonable fits, as seen in Figs. 19(a)–19(e).

Regarding the $\pi\eta - K\bar{K}$ s -wave scattering amplitude that includes the $a_0(980)$ pole, we consider two experimental inputs. First, our $a_0(980)$ propagator [$\tau_{R',R}^{LI}$ in Eq. (A7)] is fitted to the denominator of the $a_0(980)$ amplitude [Eq. (4) of Ref. [60]] from the BESIII amplitude analysis of $\chi_{c1} \rightarrow \eta\pi^+\pi^-$. Second, the ratio of coupling strengths

TABLE II. Description of two-meson scattering models. Partial waves are specified by the orbital angular momentum L and isospin I .

R	$\{L, I\}$	Number of bare states	Contact interaction	R -decay channels	Number of poles
f_0	$\{0, 0\}$	2	$\pi\pi, K\bar{K} \rightarrow \pi\pi, K\bar{K}$	$\pi\pi, K\bar{K}$	3
$\rho(770)$	$\{1, 1\}$	1	...	$\pi\pi$	1
$\kappa (K_0^*(700))$	$\{0, 1/2\}$	1	$K\pi \rightarrow K\pi$	$K\pi$	1
...	$\{0, 3/2\}$	0	$K\pi \rightarrow K\pi$...	0
$K^*(892)$	$\{1, 1/2\}$	1	$K\pi \rightarrow K\pi$	$K\pi$	1
$a_0(980)$	$\{0, 1\}$	1	...	$\eta\pi, K\bar{K}$	1
$a_2(1320)$	$\{2, 1\}$	1	...	$\eta\pi, K\bar{K}, \rho(770)\pi$	1

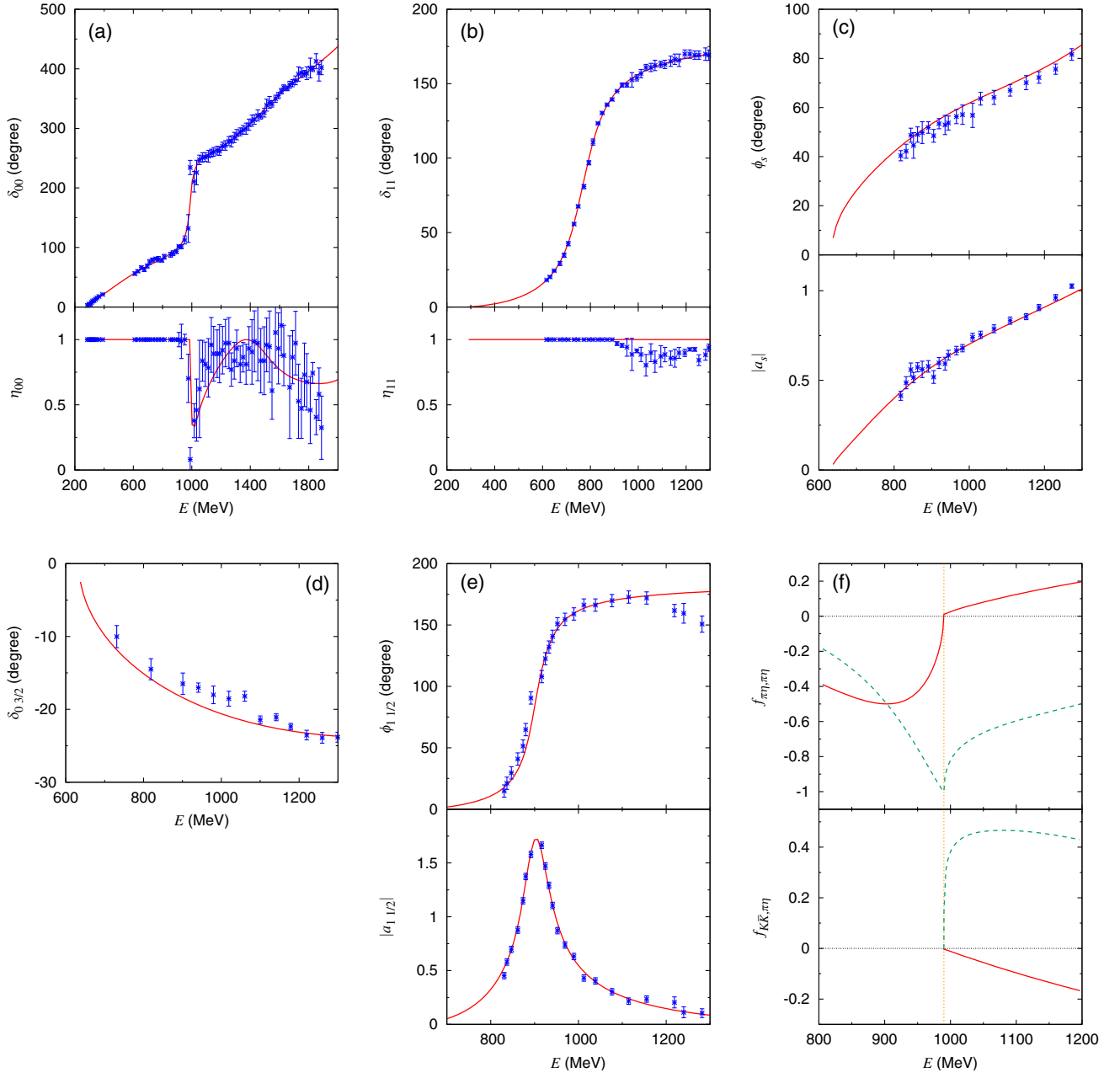


FIG. 19. (a)–(b): $\pi\pi$ scattering. Phase shifts and inelasticities are shown in the upper and lower panels, respectively. Data are from Refs. [55–57]. (a) $\{L, I\} = \{0, 0\}$; (b) $\{L, I\} = \{1, 1\}$. (c), (e): $\pi\bar{K}$ scattering. The phase and modulus of the amplitudes are shown in the upper and lower panels, respectively. Data are from Ref. [58]. (c) $L = 0$ for π^+K^- ; (e) $\{L, I\} = \{1, 1/2\}$. (d) Phase shifts of the πK scattering for $\{L, I\} = \{0, 3/2\}$; data are from Ref. [59]. (f) $\pi\eta \rightarrow \pi\eta$ (upper) and $\pi\eta \rightarrow K\bar{K}$ (lower) scattering amplitudes; $\{L, I\} = \{0, 1\}$. The real and imaginary parts are shown by the red solid and green dashed curves, respectively. The dotted vertical line indicates the $K\bar{K}$ threshold.

(including the form factor) between the $a_0(980) \rightarrow \pi\eta$ and $a_0(980) \rightarrow K\bar{K}$ is fitted to an empirical value of 1.03 from Ref. [46]. Furthermore, the relative phase between the $\pi\eta \rightarrow \pi\eta$ and $\pi\eta \rightarrow K\bar{K}$ amplitudes is chosen to be consistent with those from the chiral unitary model [61]. In Fig. 19(f), we show our $\pi\eta \rightarrow \pi\eta$ and $\pi\eta \rightarrow K\bar{K}$ scattering amplitudes defined by

$$f_{a'b',ab}^{LI}(E) = \pi \sqrt{\rho_{a'b'}} \mathcal{B}_{a'b'} \sqrt{\rho_{ab}} \mathcal{B}_{ab} T_{a'b',ab}^{LI}(q'_o, q_o; E). \quad (\text{A11})$$

Finally, we obtain the $\pi\eta - K\bar{K} - \rho\pi$ d -wave scattering amplitude with the $a_2(1320)$ pole by adjusting the model parameters so that the mass and width of $a_2(1320)$ and branching fractions of $a_2(1320) \rightarrow \pi\eta$ and $a_2(1320) \rightarrow K\bar{K}$

are reproduced; all of the fitted $a_2(1320)$ properties are from the PDG listing [15].

From the obtained partial-wave amplitudes, resonance poles are extracted and presented in Tables III–V. Overall, the pole locations are consistent with those listed in the PDG [15]. Numerical values of the fitting parameters are given in Tables VI–VIII.

TABLE III. Pole positions (M_{pole}) in our $\pi\pi$ scattering amplitudes. The RSs of the pole positions are specified by $(s_{\pi\pi}, s_{K\bar{K}})$, where $s_x = p(u)$ indicates that a pole is on the physical (unphysical) sheet of the channel x ; “–” indicates no coupling to the channel.

$\{L, I\}$	M_{pole} (MeV)	RS	Name
$\{0, 0\}$	$438 - 311i$	(up)	σ
	$1000 - 20i$	(up)	$f_0(980)$
	$1420 - 224i$	(uu)	$f_0(1370)$
$\{1, 1\}$	$769 - 78i$	$(u-)$	$\rho(770)$

TABLE IV. Pole positions (M_{pole}) in our πK scattering amplitudes. The RSs of the pole positions are specified by $(s_{\pi K})$.

$\{L, I\}$	M_{pole} (MeV)	RS	Name
$\{0, 1/2\}$	$665 - 297i$	(u)	κ
$\{1, 1/2\}$	$902 - 30i$	(u)	$K^*(892)$

TABLE V. Pole positions (M_{pole}) in our $\pi\eta$ scattering amplitudes. The RSs of the pole positions are specified by $(s_{\pi\eta}, s_{K\bar{K}}, s_{\rho\pi})$.

$\{L, I\}$	M_{pole} (MeV)	RS	Name
$\{0, 1\}$	$1070 - 112i$	$(up-)$	$a_0(980)$
$\{2, 1\}$	$1322 - 56i$	(uuu)	$a_2(1320)$

TABLE VI. Parameter values for the πK partial-wave scattering models. The i th bare R state (R_i) has a mass of m_{R_i} , and it decays into h_1 and h_2 particles with couplings (g_{h_1, h_2, R_i}) and cutoffs (c_{h_1, h_2, R_i}). Couplings and cutoffs for contact interactions are denoted by h_{h_1, h_2, h_1, h_2} and b_{h_1, h_2} , respectively. The parameters are defined in Eqs. (A1), (A2), (A6), and (7). For simplicity, we suppress the superscripts LI of the parameters. The mass and cutoff values are given in units of MeV, and the couplings are dimensionless.

$R\{L, I\}$	$\kappa(K_0^*) \{0, 1/2\}$	$\{0, 3/2\}$	$K^* \{1, 1/2\}$
m_{R_1}	1239	...	926
$g_{\pi\bar{K}, R_1}$	5.79	...	0.74
$c_{\pi\bar{K}, R_1}$	1000	...	752
$h_{\pi\bar{K}, \pi\bar{K}}$	0.59	0.47	-0.01
$b_{\pi\bar{K}}$	1000	1973	752

TABLE VII. Parameter values for the $\pi\pi$ partial-wave scattering models. See Table VI for the description.

$R\{L, I\}$	$f_0 \{0, 0\}$	$\rho \{1, 1\}$
m_{R_1}	1007	834
$g_{\pi\pi, R_1}$	6.76	1.03
$c_{\pi\pi, R_1}$	1458	1040
$g_{K\bar{K}, R_1}$	-4.75	...
$c_{K\bar{K}, R_1}$	711	...
m_{R_2}	1677	...
$g_{\pi\pi, R_2}$	-5.87	...
$c_{\pi\pi, R_2}$	1458	...
$g_{K\bar{K}, R_2}$	10.21	...
$c_{K\bar{K}, R_2}$	711	...
$h_{\pi\pi, \pi\pi}$	0.65	...
$h_{\pi\pi, K\bar{K}}$	-0.42	...
$h_{K\bar{K}, K\bar{K}}$	-1.11	...
$b_{\pi\pi}$	1458	...
$b_{K\bar{K}}$	711	...

TABLE VIII. Parameter values for the $\pi\eta$ partial-wave scattering models. See Table VI for the description.

$R\{L, I\}$	$a_0 \{0, 1\}$	$a_2 \{2, 1\}$
m_{R_1}	1233	1436
$g_{\pi\eta, R_1}$	-3.08	0.09
$c_{\pi\eta, R_1}$	1973	1000
$g_{K\bar{K}, R_1}$	2.94	0.07
$c_{K\bar{K}, R_1}$	1973	1000
$g_{\rho\pi, R_1}$...	0.33
$c_{\rho\pi, R_1}$...	1000

APPENDIX B: PARAMETERS FITTED TO RADIATIVE J/ψ DECAY DATA

Table IX presents model parameters determined by fitting $J/\psi \rightarrow \gamma(0^{-+}) \rightarrow \gamma(K_S K_S \pi^0)$ Dalitz plot pseudodata and the branching fractions of $\eta(1405/1475) \rightarrow \eta\pi^+\pi^-$ and $\eta(1405/1475) \rightarrow \rho^0\gamma$ relative to that of $\eta(1405/1475) \rightarrow K\bar{K}\pi$. When a two-meson scattering model includes contact interactions, we consider a direct bare $M^* \rightarrow abc$ decay where two pseudoscalar mesons (ab) have an orbital angular momentum L and a total isospin I . We describe this bare vertex function with [cf. Eq. (12)]

$$F_{(c(ab)_{LI})_I, M_i^*}(q) = C_{(c(ab)_{LI})_I}^{M_i^*} \left(\frac{q}{m_\pi} \right)^l \times \frac{[1 + q^2 / (\Lambda_{(c(ab)_{LI})_I}^{M_i^*})^2]^{-2-\frac{l}{2}}}{\sqrt{4E_c(q)m_{M_i^*}}}, \quad (\text{B1})$$

TABLE IX. Parameter values for i th bare η^* state obtained from one of the bootstrap fits. The symbols are the $J/\psi\eta_i^*\gamma$ coupling constant $g_{J/\psi\eta_i^*\gamma}$ in Eq. (4), the bare mass $m_{\eta_i^*}$ in Eq. (15), and bare couplings $C_{cR^n}^i$ in Eq. (12) and $C_{c(ab)_{LI}}^i$ in Eq. (B1); the subscripts l are suppressed. R^n stands for the n th bare R state, while $(ab)_{LI}$ is a direct decay into two pseudoscalar mesons (ab) with the orbital angular momentum L and total isospin I . The nonresonant amplitude parameter c_{NR} has been introduced in Eq. (27). Since the overall normalization of the full amplitude is arbitrary in our model, a common scaling factor can be multiplied to $g_{J/\psi\eta_i^*\gamma}$ and c_{NR} . All cutoffs [$\Lambda_{cR^n}^i$ in Eq. (12) and $\Lambda_{c(ab)_{LI}}^i$ in Eq. (B1)] are fixed to 700 MeV.

$m_{\eta_1^*}$ (MeV)	1622	$m_{\eta_2^*}$ (MeV)	2309
$g_{J/\psi\eta_1^*\gamma}$	1 (fixed)	$g_{J/\psi\eta_2^*\gamma}$	$0.317 - 0.454i$
$C_{\bar{K}K^*}^1$	2.00	$C_{\bar{K}K^*}^2$	4.54
$C_{\bar{K}(\pi K)_{\frac{1}{2}}}^1$	-0.421	$C_{\bar{K}(\pi K)_{\frac{1}{2}}}^2$	-0.124
$C_{\bar{K}\kappa}^1$	19.4	$C_{\bar{K}\kappa}^2$	22.6
$C_{\bar{K}(\pi K)_{\frac{0}{2}}}^1$	3.10	$C_{\bar{K}(\pi K)_{\frac{0}{2}}}^2$	2.19
$C_{\pi a_0}^1$	-1.01	$C_{\pi a_0}^2$	-1.15
$C_{\pi a_2}^1$	2.38	$C_{\pi a_2}^2$	-3.12
$C_{\eta f_0^1}^1$	-2.40	$C_{\eta f_0^1}^2$	-7.28
$C_{\eta f_0^2}^1$	-1.33	$C_{\eta f_0^2}^2$	9.26
$C_{\eta(\pi\pi)_{00}}^1$	0.358	$C_{\eta(\pi\pi)_{00}}^2$	3.10
$C_{\eta(KK)_{00}}^1$	0 (fixed)	$C_{\eta(KK)_{00}}^2$	0 (fixed)
$C_{\rho\rho}^1$	0 (fixed)	$C_{\rho\rho}^2$	44.9
c_{NR} (GeV^{-2})	$127 - 41i$		

where $C_{c(ab)_{LI}}^{M_i^*}$ and $\Lambda_{c(ab)_{LI}}^{M_i^*}$ are coupling and cutoff parameters, respectively. This bare vertex function is used in a dressed vertex and a self-energy in a similar manner as the bare vertex $F_{(cR)_l, M_i^*}$ in Eq. (12) is used in Eqs. (10), (11), and (16).

-
- [1] P.H. Baillon, D. Edwards, B. Marechal, L. Montanet, M. Tomas, C. d'Andlau, A. Astier, J. Cohen-Ganouna, M. Della-Negra, S. Wojcicki *et al.*, Further study of the e -meson in antiproton proton annihilation at rest, *Nuovo Cimento A* **50**, 393 (1967).
- [2] C. Amsler *et al.*, Production and decay of $\eta'(958)$ and $\eta(1440)$ in $p\bar{p}$ annihilation at rest, *Eur. Phys. J. C* **33**, 23 (2004).
- [3] T. Bolton *et al.*, Partial-wave analysis of $J/\psi \rightarrow \gamma\eta\pi^+\pi^-$, *Phys. Rev. Lett.* **69**, 1328 (1992).
- [4] J.-Z. Bai *et al.* (BES Collaboration), Partial wave analysis of $J/\psi \rightarrow \gamma(\eta\pi^+\pi^-)$, *Phys. Lett. B* **446**, 356 (1999).
- [5] J.-E. Augustin *et al.* (DM2 Collaboration), Radiative decay of J/ψ into $\eta(1430)$ and nearby states, *Phys. Rev. D* **42**, 10 (1990).
- [6] M. Ablikim *et al.* (BESIII Collaboration), $\eta\pi^+\pi^-$ resonant structure around $1.8\text{ GeV}/c^2$ and $\eta(1405)$ in $J/\psi \rightarrow \omega\eta\pi^+\pi^-$, *Phys. Rev. Lett.* **107**, 182001 (2011).
- [7] M. Acciarri *et al.* (L3 Collaboration), Light resonances in $K_S^0 K^\pm \pi^\mp$ and $\eta\pi^+\pi^-$ final states in $\gamma\gamma$ collisions at LEP, *Phys. Lett. B* **501**, 1 (2001).
- [8] J.Z. Bai *et al.* (BES Collaboration), A study of $J/\psi \rightarrow \gamma\gamma V(\rho, \phi)$ decays with the BESII detector, *Phys. Lett. B* **594**, 47 (2004).
- [9] D. Coffman *et al.* (MARK-III Collaboration), Study of the doubly radiative decay $J/\psi \rightarrow \gamma\gamma\rho^0$, *Phys. Rev. D* **41**, 1410 (1990).
- [10] G.S. Adams *et al.* (E852 Collaboration), Observation of pseudoscalar and axial vector resonances in $\pi^- p \rightarrow K^+ K^- \pi^0 n$ at 18 GeV, *Phys. Lett. B* **516**, 264 (2001).
- [11] M.G. Rath *et al.*, The $K_S^0 K_S^0 \pi^0$ system produced in $\pi^- p$ interactions at 21.4 GeV/c, *Phys. Rev. D* **40**, 693 (1989).
- [12] F. Nichituiu *et al.* (OBELIX Collaboration), Study of the $K^+ K^- \pi^+ \pi^- \pi^0$ final state in antiproton annihilation at rest in gaseous hydrogen at NTP with the OBELIX spectrometer, *Phys. Lett. B* **545**, 261 (2002).
- [13] Z. Bai *et al.* (MARKIII Collaboration), Partial-wave analysis of $J/\psi \rightarrow \gamma K_S^0 K^\pm \pi^\mp$, *Phys. Rev. Lett.* **65**, 2507 (1990).
- [14] J.-E. Augustin *et al.* (DM2 Collaboration), Partial-wave analysis of DM2 Collaboration data in the $\eta(1430)$ energy range, *Phys. Rev. D* **46**, 1951 (1992).

- [15] P. A. Zyla *et al.* (Particle Data Group), The review of particle physics, *Prog. Theor. Exp. Phys.* **2020**, 083C01 (2020).
- [16] T. Barnes, F.E. Close, P.R. Page, and E.S. Swanson, Higher quarkonia, *Phys. Rev. D* **55**, 4157 (1997).
- [17] L. Faddeev, A. J. Niemi, and U. Wiedner, Glueballs, closed fluxtubes, and $\eta(1440)$, *Phys. Rev. D* **70**, 114033 (2004).
- [18] G. S. Bali, K. Schilling, A. Hulsebos, A. C. Irving, C. Michael, and P. W. Stephenson (UKQCD Collaboration), A comprehensive lattice study of SU(3) glueball, *Phys. Lett. B* **309**, 378 (1993).
- [19] C. J. Morningstar and M. J. Peardon, Glueball spectrum from an anisotropic lattice study, *Phys. Rev. D* **60**, 034509 (1999).
- [20] Y. Chen, A. Alexandru, S. J. Dong, T. Draper, I. Horváth, F. X. Lee, K. F. Liu, N. Mathur *et al.*, Glueball spectrum and matrix elements on anisotropic lattices, *Phys. Rev. D* **73**, 014516 (2006).
- [21] C. M. Richards, A. C. Irving, E. B. Gregory, and C. McNeile (UKQCD Collaboration), Glueball mass measurements from improved staggered fermion simulations, *Phys. Rev. D* **82**, 034501 (2010).
- [22] F. Chen, X. Jiang, Y. Chen, K.-F. Liu, W. Sun, and Y.-B. Yang, Glueballs at physical pion mass, *Chin. Phys. C* **47**, 063108 (2023).
- [23] J. J. Dudek, R. G. Edwards, P. Guo, and C. E. Thomas (Hadron Spectrum Collaboration), Toward the excited isoscalar meson spectrum from lattice QCD, *Phys. Rev. D* **88**, 094505 (2013).
- [24] M. Ablikim *et al.* (BESIII Collaboration), First observation of $\eta(1405)$ decays into $f_0(980)\pi^0$, *Phys. Rev. Lett.* **108**, 182001 (2012).
- [25] J.-J. Wu, X.-H. Liu, Q. Zhao, and B.-S. Zou, Puzzle of anomalously large isospin violations in $\eta(1405/1475) \rightarrow 3\pi$ in the J/ψ radiative decay, *Phys. Rev. Lett.* **108**, 081803 (2012).
- [26] X.-G. Wu, J.-J. Wu, Q. Zhao, and B.-S. Zou, Understanding the property of $\eta(1405/1475)$ in the J/ψ radiative decay, *Phys. Rev. D* **87**, 014023 (2013).
- [27] F. Aceti, W. H. Liang, E. Oset, J. J. Wu, and B. S. Zou, Isospin breaking and $f_0(980)$ - $a_0(980)$ mixing in the $\eta(1405) \rightarrow \pi^0 f_0(980)$ reaction, *Phys. Rev. D* **86**, 114007 (2012).
- [28] M.-C. Du and Q. Zhao, Internal particle width effects on the triangle singularity mechanism in the study of the $\eta(1405)$ and $\eta(1475)$ puzzle, *Phys. Rev. D* **100**, 036005 (2019).
- [29] M. Ablikim *et al.* (BESIII Collaboration), Study of $\eta(1405)/\eta(1475)$ in $J/\psi \rightarrow \gamma K_S^0 K_S^0 \pi^0$ decay, *J. High Energy Phys.* **03** (2023) 121.
- [30] S. X. Nakamura, H. Kamano, T.-S. H. Lee, and T. Sato, Extraction of meson resonances from three-pions photoproduction reactions, *Phys. Rev. D* **86**, 114012 (2012).
- [31] S. X. Nakamura, Q. Huang, J.-J. Wu, H. P. Peng, Y. Zhang, and Y. C. Zhu, Three-body unitary coupled-channel analysis on $\eta(1405/1475)$, *Phys. Rev. D* **107**, L091505 (2023).
- [32] F. Niecknig, B. Kubis, and S. P. Schneider, Dispersive analysis of $\omega \rightarrow 3\pi$ and $\phi \rightarrow 3\pi$ decays, *Eur. Phys. J. C* **72**, 2014 (2012).
- [33] I. V. Danilkin, C. Fernández-Ramírez, P. Guo, V. Mathieu, D. Schott, M. Shi, and A. P. Szczepaniak, Dispersive analysis of $\omega/\phi \rightarrow 3\pi, \pi\gamma^*$, *Phys. Rev. D* **91**, 094029 (2015).
- [34] S. X. Nakamura, Coupled-channel analysis of $D^+ \rightarrow K^-\pi^+\pi^+$ decay, *Phys. Rev. D* **93**, 014005 (2016).
- [35] H. Kamano, S. X. Nakamura, T.-S. H. Lee, and T. Sato, Unitary coupled-channels model for three-mesons decays of heavy mesons, *Phys. Rev. D* **84**, 114019 (2011).
- [36] M. Mai, B. Hu, M. Döring, A. Pilloni, and A. Szczepaniak, Three-body unitarity with isobars revisited, *Eur. Phys. J. A* **53**, 177 (2017).
- [37] M. Mikhasenko, Y. Wunderlich, A. Jackura, V. Mathieu, A. Pilloni, B. Ketzner, and A. P. Szczepaniak, Three-body scattering: Ladders and resonances, *J. High Energy Phys.* **08** (2019) 080.
- [38] W. Glöckle, S-matrix pole trajectory in a three-neutron model, *Phys. Rev. C* **18**, 564 (1978).
- [39] B. C. Pearce and I. R. Afnan, Resonance poles in three-body systems, *Phys. Rev. C* **30**, 2022 (1984).
- [40] G. Janssen, K. Holinde, and J. Speth, Meson exchange model for $\pi\rho$ scattering, *Phys. Rev. C* **49**, 2763 (1994).
- [41] M. Mikhasenko, A. Pilloni, M. Albaladejo, C. Fernández-Ramírez, A. Jackura, V. Mathieu, J. Nys, and A. Rodas, B. Ketzner, and A. P. Szczepaniak (JPAC Collaboration), Pole position of the $a_1(1260)$ from τ -decay, *Phys. Rev. D* **98**, 096021 (2018).
- [42] D. Sadasivan, A. Alexandru, H. Akdag, F. Amorim, R. Brett, C. Culver, M. Döring, F. X. Lee, and M. Mai, Pole position of the $a_1(1260)$ resonance in a three-body unitary framework, *Phys. Rev. D* **105**, 054020 (2022).
- [43] M. Bando, T. Kugo, and K. Yamawaki, Nonlinear realization and hidden local symmetries, *Phys. Rep.* **164**, 217 (1988).
- [44] D. Bisello *et al.* (DM2 Collaboration), First observation of three pseudoscalar states in the $J/\psi \rightarrow \gamma\rho\rho$ decay, *Phys. Rev. D* **39**, 701 (1989).
- [45] W. H. Press, S. A. Teukolsky, W. T. Vetterling, and B. P. Flannery, *Numerical Recipes 3rd Edition: The Art of Scientific Computing* 3rd ed. (Cambridge University Press, New York, NY, USA, 2007).
- [46] A. Abele *et al.*, $\bar{p}p$ annihilation at rest into $K_L K^\pm \pi^\mp$ *Phys. Rev. D* **57**, 3860 (1998).
- [47] M. Ablikim *et al.* (BESIII Collaboration), Observation of an a_0 -like state with mass of 1.817 GeV in the study of $D_s^+ \rightarrow K_S^0 K^+ \pi^0$ decays, *Phys. Rev. Lett.* **129**, 182001 (2022).
- [48] D. Barberis *et al.* (WA102 Collaboration), A measurement of the branching fractions of the $f_1(1285)$ and $f_1(1420)$ produced in central pp interactions at 450 GeV/c, *Phys. Lett. B* **440**, 225 (1998).
- [49] J. Lu and B. Moussallam, The $\pi\eta$ interaction and a_0 resonances in photon-photon scattering, *Eur. Phys. J. C* **80**, 436 (2020).
- [50] N. Suzuki, T. Sato, and T.-S. H. Lee, Extraction of electromagnetic transition form factors for nucleon resonances within a dynamical coupled-channels model, *Phys. Rev. C* **82**, 045206 (2010).
- [51] M. Ablikim *et al.* (BESIII Collaboration), Study of $\psi(3686) \rightarrow \omega K \bar{K} \pi$ decays, *Phys. Rev. D* **87**, 092006 (2013).

- [52] M. Ablikim *et al.* (BESIII Collaboration), Measurement of branching fractions of $\psi(3686) \rightarrow \phi\eta'$, $\phi f_1(1285)$ and $\phi\eta(1405)$, *Phys. Rev. D* **100**, 092003 (2019).
- [53] M. Ablikim *et al.* (BESIII Collaboration), $\eta\pi^+\pi^-$ resonant structure around 1.8 GeV/c² and $\eta(1405)$ in $J/\psi \rightarrow \omega\eta\pi^+\pi^-$, *Phys. Rev. Lett.* **107**, 182001 (2011).
- [54] M. Ablikim *et al.* (BESIII Collaboration), Measurements of J/ψ decays into $\omega K\bar{K}\pi$, $\phi K\bar{K}\pi$, and $\eta K_S^0 K^\pm \pi^\mp$, *Phys. Rev. D* **77**, 032005 (2008).
- [55] G. Grayer *et al.*, High statistics study of the reaction $\pi^- p \rightarrow \pi^- \pi^+ n$: Apparatus, method of analysis, and general features of results at 17 GeV/c, *Nucl. Phys.* **B75**, 189 (1974).
- [56] B. Hyams *et al.*, $\pi\pi$ phase-shift analysis from 600 to 1900 MeV, *Nucl. Phys.* **B64**, 134 (1973).
- [57] J. R. Batley *et al.* (The NA48/2 Collaboration), New high statistics measurement of K_{e4} decay form factors and $\pi\pi$ scattering phase shifts, *Eur. Phys. J. C* **54**, 411 (2008).
- [58] D. Aston *et al.*, A study of $K^-\pi^+$ scattering in the reaction $K^- p \rightarrow K^-\pi^+ n$ at 11 GeV/c, *Nucl. Phys.* **B296**, 493 (1988).
- [59] P. Estabrooks *et al.*, Study of $K\pi$ scattering using the reactions $K^\pm p \rightarrow K^\pm \pi^+ n$ and $K^\pm p \rightarrow K^\pm \pi^- \Delta^{++}$ at 13 GeV, *Nucl. Phys.* **B133**, 490 (1978).
- [60] M. Ablikim *et al.* (BESIII Collaboration), Amplitude analysis of the $\chi_{c1} \rightarrow \eta\pi^+\pi^-$ decays, *Phys. Rev. D* **95**, 032002 (2017).
- [61] J. A. Oller and E. Oset, Chiral symmetry amplitudes in the S -wave isoscalar and isovector channels and the σ , $f_0(980)$, $a_0(980)$ scalar mesons, *Nucl. Phys.* **A620**, 438 (1997).